Application of Computational Thermodynamic and Solidification Kinetics to Cold Sprayable Powder Alloy Design

DANIELLE BELSITO

January 14, 2014

ABSTRACT

Military aircraft that require high maneuverability, durability, ballistic protection, reparability, and energy efficiency require structural alloys with low density, high toughness, and high strength. Also, repairs to these aircraft demand a production process that has the flexibility to be relatively in-situ with the same high-performance output. Materials produced by the cold spray process, a thermo-mechanical powder consolidation technique, meet many of the requirements.

In accordance with President Obama's 2011 Materials Genome Initiative, the focus of this effort is to design customized aluminum alloy powders which exploit the unique behavior and properties of the materials created by the cold spray process. Analytical and computational models are used to customize microchemistry, thermal conditioning, and solidification behavior of the powders by predicting equilibrium and non-equilibrium microstructure and resulting materials properties and performance. Thermodynamic, kinetic, and solidification models are used, including commercial software packages Thermo-Calc, Pandat™, and JMatPro®, and TC-PRISMA. Predicted powder properties can be used as input into a cold spray process impact model to determine the consolidated materials' properties. Mechanical properties of powder particles are predicted as a function of powder particle diameter and are compared to experimental results.

EXECUTIVE SUMMARY

THROUGH PROCESS MODEL

In industry, very little work has been done in the area of fundamentally understanding the material behavior in the cold spray process. A trial and error, guess and check method has been utilized to produce materials at or near the desired result. Not only is this method inefficient, but optimal process and material conditions may not be discovered using this method, reducing the overall success of the method.

The cold spray process involves numerous process and materials parameters throughout several stages of the process, as shown in the schematic of the current through-process model in Figure 1. Currently, each stage contains models that run independently of the models in other stages. Even operating independently, the models provide substantially useful information, such as a phase fraction in the sprayable powder as a function of degassing temperature.

When all of the individual models are operational, they will be integrated so the outputs from one stage will be used as the input for the subsequent stage. Then the user can specify the material to be sprayed, and the operating conditions will be optimized for that particular material, or final properties can be specified and alloy compositions can be altered to produce the desired properties. Additionally, the model will be able to serve as a scenario seeker, where various parameters and/or materials can be altered in the model and the final materials properties will be predicted. This will be useful to study the effect of final properties as a function of these parameters.

The powder production and powder processing stages were the sections focused on in this work. Thermodynamic, kinetic, and solidification models were used as a foundation to determine the effects of composition, solidification conditions, and heat treating techniques on the microstructure and resulting mechanical properties of the powder particles, all as a function of powder particle size.

Overall, these models significantly reduce the amount of time, money, and resources spent on trial and error-type experimentation. Currently, the powder production model is being utilized to aid in the selection of alloys with cold sprayable potential, as well as determine ideal powder particle sizes to be sprayed to produce excellent consolidated material microstructures. The powder processing model has been used to understand the effects of the degassing procedure on the bulk powder sample, and how to improve the degassing result by further altering the process parameters.

ELEMENTAL IMPACT FACTOR

As an aid to the alloy composition selection, the elemental impact factor is a quantitative way to determine the impact a given element has on any phase at a specific temperature. This is most useful when there are known beneficial or deleterious phases present in a system.

For example, if a manufactured part is observed to fail due to crack initiations at a known phase (or multiple phases), the impact factors for elements in the alloy can be calculated for that phase. Elements with a negative impact factor, meaning the addition of that element decrease the amount of phase under investigation, could be added to the system. This is especially beneficial in cases where undesired phase are caused by the presence of impurity elements which cannot be removed from the alloy.

Similarly, for the formation of desired phases, elements with a positive impact factor could be increased to promote the amount of the desired phase and elements with a negative impact factor could potentially be decreased, though the addition of elements is typically easier than the reduction of elements, unless the alloy is made from scratch.

Finally, the addition of elements not traditionally present in the alloys being used may be examined with the impact factor to determine potential eligible elements which may increase or decrease the amount of desired or deleterious elements.

In the case of all of the above examples, the desired and/or undesired phases must first be known in order to find the impact factor useful. This often requires experimental investigation into the material and its failure mechanisms. However, once these phases are known, the benefits may be great. As with many computation models, the time, resources, and monetary savings from modeling as opposed to experimentation are significant. Of course, models cannot be substituted entirely for experiments, the impact factor model can be used to determine calculated candidate chemical compositions for alloys.

POWDER MECHANICAL PROPERTIES MODEL

While part of the through process model, the powder mechanical properties model is also a standalone model that predicts the mechanical properties, (yield stress, ultimate tensile strength, and hardness) of powder particles as a function of powder particle size. Also, an experimental method was devised to compare experimental results with model-predicted output.

This model may be useful in determining powder properties as a function of powder particle size in applications where properties of individual powders, not just the bulk properties, are desired. An example obvious to this research would be the cold spray process, since the powders are not melted during processing. Other powder processes occurring without this phase transformation may also have use for this type of powder properties model.

TABLE OF CONTENTS

1 INTRODUCTION

1.1 PROJECT NEEDS

Materials used in military aircraft require a specific set of high performance properties in order to ensure the maximum protection of warfighters. These features include highly maneuverable vehicles made of highly durable and high strength materials. Also, a fuel efficient vehicle is not only cost-effective, but essential to minimizing refueling downtime. Finally, the vehicle needs to have the ability to be repaired on site, by minimally trained warfighters. This greatly improves the readability of the vehicle.

An example of the importance of reparability is the magnesium gearboxes used to house the engine(s) in military rotorcraft. Unscheduled maintenance and replacement of gearboxes in the vehicle fleet costs the Department of Defense over $100 million annually. Replacement parts require a long lead time of up to 18 months [1]. Failure to replace the gearboxes affects mission-critical flight safety equipment, reducing material strength and safety factors. This deterioration can cause loss of transmission oil and pressure, excessive heat and wear, seizing gears and, ultimately, a loss of the vehicle.

Two distinct but overlapping requirements need to be addressed. First, structural materials need to be developed with high toughness, low density, and high strength. Secondly, these materials need the capability of being repaired in-situ. One technique that allows for the simultaneous solution to these requirements is the powder cold spray process. The cold spray process is a powder consolidation technique which produces materials with significantly higher as-sprayed hardness than conventionally produced alloys. It is also adaptable to be a fully mobile process, allowing for in-situ repairs.

There has been little research in the selection and/or design of powders specifically for use in the cold spray process. Powders need to be designed to maximize the unique behavior of the cold spray process to produce exceptionally high performing materials.

1.2 PROJECT GOALS

The goal of this work was to model the microstructure and resulting mechanical properties of alloy powders to be used as input into a cold spray powder impact model, producing properties of the consolidated material. In addition to commercially available alloys, custom tailored alloy powders were developed to exploit the unique behavior of the cold spray process to produce exceptional materials to be used on military aircraft.

The powder design was not exclusive from the rest of the cold spray process. In fact, in order to understand the needs of the powder properties, attention needed to be paid to the entire process. The cold spray process was separated into five distinct research areas and a through-process model was developed, similar to those employed on other complex processes [2-5]. A schematic of the five stages of the through process model is shown in Figure 1.

While the goal of the entire ARL@WPI group is to model the complete through-process, areas focused on in this research included the powder production and powder processing areas. An overview of the entire through process model is, however, given in Section 3.

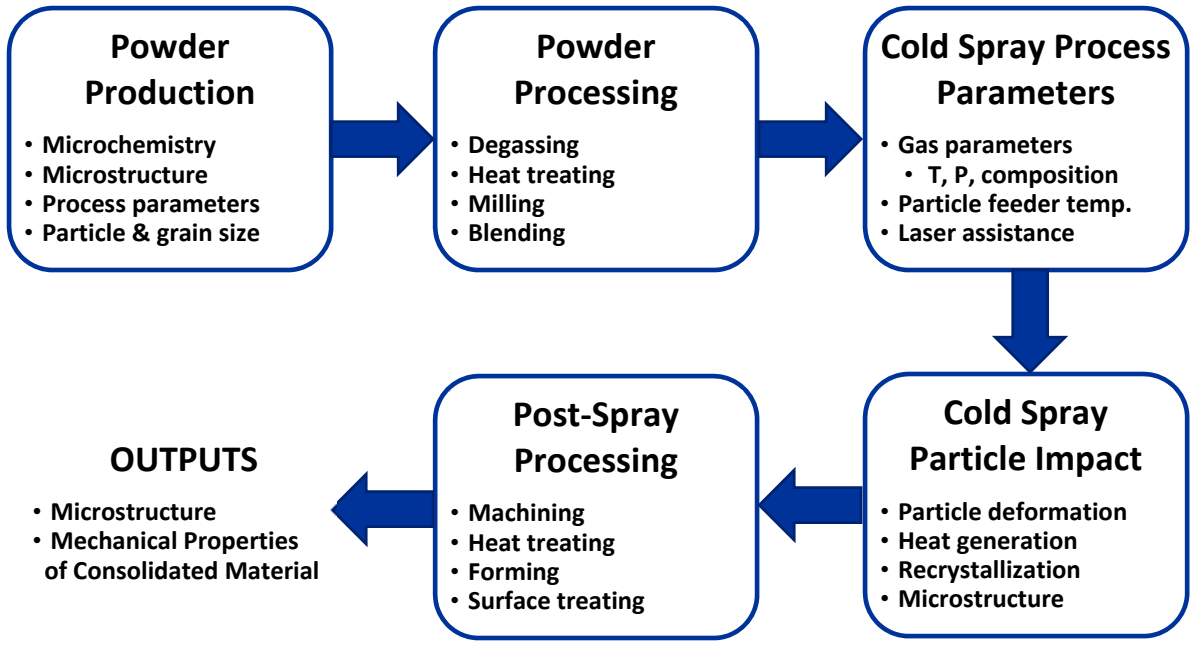

Figure 1. Through-process model of the cold spray process modeling efforts at ARL@MPI.

One unique feature of the cold spray process, as its name suggests, is that the material used in the process remains relatively cold; the temperature of the process never exceeds the melting temperature of the powder that is sprayed. The majority of processes involving powder alloys require complete melting of the powder. During melting, the thermal history and microstructure of the powder are irrelevant, since the powder is completely homogenized on heating. As a result, little research has been done on the properties and microstructure of the powder. The goal of this research was to focus on powder production and pre-cold spray processing stages 1) model the microstructural features and resulting mechanical properties and 2) use this model to design powders with features that will best enhance materials created using the cold spray process. Powder particle size, microchemistry, microstructure, and thermal processing are part of the designed powder parameters.

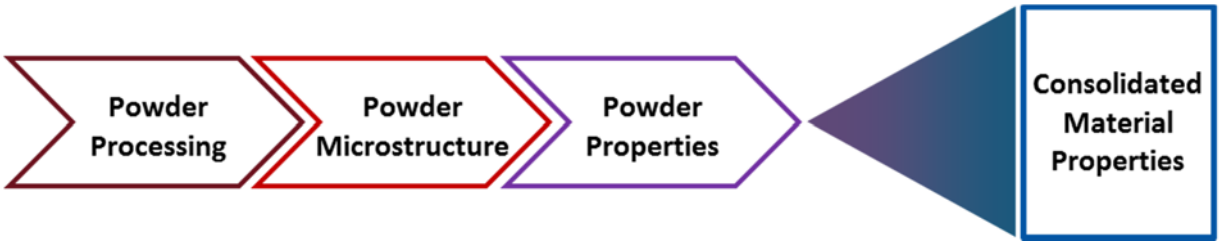

Figure 2. Schematic showing the effect powder properties have on the cold spray consolidated material.

Figure 2 graphically depicts the importance of the powder processing stage in the overall behavior of the cold spray consolidated material. The material properties of the consolidated material are directly dependent on the properties of the powder, which are dependent on the powder microstructure, which is determined by the powder processing parameters.

1.3 BACKGROUND

The cold spray process is a powder consolidation process in which powder particles are injected into a heated, high velocity inert gas stream. The particle-carrying gas is accelerated to supersonic velocities through a de Laval nozzle onto a substrate. Due to the high velocity of the particles they are plastically deformed upon impact, causing them to adhere to the substrate undergoing severe plastic deformation. As the process continues, the sprayed material thickness increases. [6, 7] A schematic of the cold spray process is given in Figure 3.

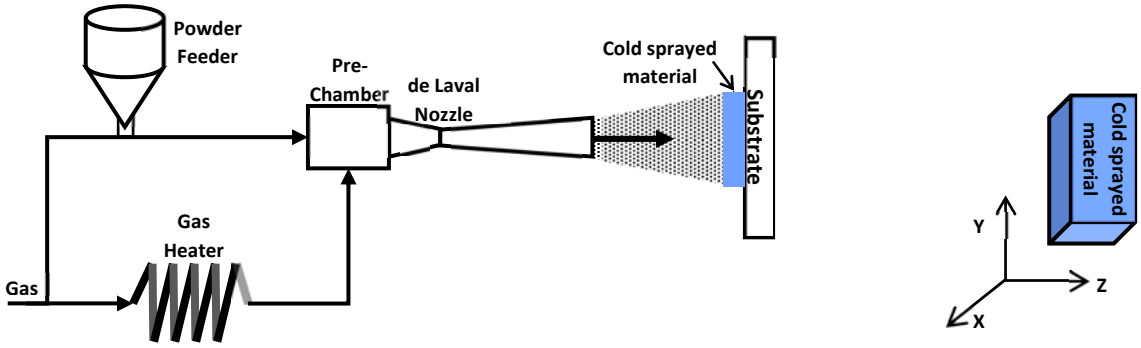

Figure 3. Left: Schematic of the cold spray process. Right: Directional faces of a cold sprayed material with Z as the spray direction.

A primary advantage of the cold spray process is that the temperature of the powder and consolidated material never exceed the melting temperature of the material. This results in minimal particle oxidation and minimal tensile stresses due to thermal contraction. Also, due to the dynamic nature of the process, the resulting consolidated material has extremely low porosity with near 100% wrought/cast alloy density, and primarily compressive stresses. Perhaps the greatest feature cold sprayed materials have are their extremely high hardness. Depending on processing conditions, the hardness values of as-sprayed material is greater than two times harder than a respective wrought alloy.

The cold spray process is currently used to fabricate structural bulk materials as well as cosmetic and functional coatings. It can be used to make near-net shapes, producing little waste. Major applications of cold spraying are for defect repairs and substrate corrosion protection. [6]

1.4 ALLOYS USED

The alloys used in this project were all aluminum based and in the 5xxx and 6xxx series. The specific alloys were selected by the U.S. Army Research Laboratory. Composition specifications are given in Table 1.

Table 1. Specification chemical compositions of the alloys discussed, given in weight percent. [8, 9]

Wt%	Al	Cr	Cu	Fe	Mg	Mn	Si	Ti	Zn
Al 5056	Balance	0.05 - 0.2	0 - 0.1	0 - 0.4	4.5 - 5.6	0.05 - 0.2	0 - 0.3	-	0 - 0.1
Al 5083	Balance	0 - 0.1	0.05 - 0.25	0 - 0.4	4 - 4.9	0.4 - 1	0 - 0.4	0 - 0.15	0 - 0.25
Clean Al 5083	Balance	-	-	0.05	3.4	0.44	0.06	-	-
Al 6061	Balance	0.04 - 0.35	0.15 - 0.4	0 - 0.7	0.8 - 1.2	0 - 0.15	0.4 - 0.8	0 - 0.15	0 - 0.25

Al 5056, Al 5083, and Al 6061 are commercially available alloys. Clean Al 5083 is a custom designed alloy with lower impurity element concentrations; there is significantly less Fe and Si in clean Al 5083 than conventional Al 5083.

2 LITERATURE REVIEW

2.1 LITERATURE REVIEW SUMMARY

The cold spray process was developed in Russia the 1980's [6]. Research has been done on the optimization of cold spray processing parameters, the effects of spraying various alloy and composite powders, and the applications of the cold spray process. Limited work has been done on the microstructural characterization of materials consolidated using the cold spray process. Even less, if any, has been done on designing alloys with the specific intention of use in the cold spray process. General materials by design work is summarized in Section 2.2, as well as specifics on thermodynamic, kinetic, and powder solidification modeling in Sections 2.3, 2.4, and 2.5, respectfully.

2.2 MATERIALS BY DESIGN LITERATURE REVIEW

Before the development of materials software modeling packages, hand-written analytical methods were used to crudely model and predict the behavior of alloys. A more common approach, however, was the time and cost ineffective, inefficient use of trial-and-error to design novel alloys. Computational software packages have since replaced many trial-and-error operations, and materials are being developed at a significantly faster pace, and at a lower cost.

This is precisely why U.S. President Obama initiated the Materials Genome Initiative (MGI) for Global Competitiveness in 2011, so that the "development of advanced materials can be accelerated through advances in computational techniques." [10]

> *"The lengthy time frame for materials to move from discovery to market is due in part to the continued reliance of materials research and development programs on scientific intuition and trial and error experimentation. Much of the design and testing of materials is currently performed through time-consuming and repetitive experiment and characterization loops. Some of these experiments could potentially be performed virtually with powerful and accurate computational tools, but that level of accuracy in such simulations does not yet exist."*
>
> **Materials Genome Initiative** (2011) [10]

While one part of the Materials Genome Initiative is to develop a more efficient portal to share data, the other area is the rapid innovation of novel materials by computation modeling. Currently, new materials are designed and developed using the stages in the schematic shown in Figure 4. This is an inefficient and often ineffective method for materials development. The computational materials science approach outlined in the Initiative is proposed to shorten the new material development lifetime from 10-20 years to two to three years. [10]

The MGI report specifically notes the use by the Department of Defense laboratories of modeling to develop "lightweight protection materials." In this work, computation models in the specific areas of thermodynamic, kinetic, and solidification will be utilized to design alloys for this specific purpose.

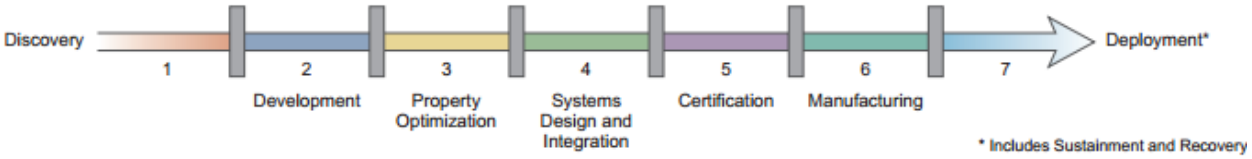

Figure 4. Traditional process of material development, as described in the Materials Genome Initiative. [10]

Extensive work in the materials by design area has been performed by G. Olson at Northwestern University and QuesTek Innovations. [11-13] An example of successful materials by design, Olson developed a new commercial steel to serve as corrosion resistant landing gear material, Ferrium S53, using computational modeling to design and develop the alloy in significantly less time than conventional empirical design approaches would take. Competing material requirements were weighted and tradeoffs were made to systematically develop optimal materials. [11]

2.3 Thermodynamic Modeling Literature Review

Experimental work, which will be discussed in a later section, has shown that the microstructure and microchemistry of the powder used in the cold spray process is almost identical to that found in the cold sprayed consolidated material. Also, the cold spray process occurs at temperatures below the melting temperature of the material. This allows for initial predictive modeling to be performed simply on the powder alloy, then altered with particle impact model in a later stage of the through-process model to determine the final microstructure of the cold spray consolidated material.

Numerous software packages utilize the CALPHAD, CALculation of PHase Diagram, approach of thermodynamic modeling. [14] Thermodynamic models presented here utilized Pandat, Thermo-Calc, and JMatPro software packages. While thermodynamic models provided useful equilibrium data, they could not be used solely to predict the complete behavior of a system; kinetic considerations needed to be made since materials are typically not present in equilibrium states.

Thermodynamic models predict data that can, however, be used in conjunction with kinetic and solidification models to produce a more accurate prediction. In order to model many kinetic phenomenon, thermodynamic parameters are required. For example, chemical potential from thermodynamic predictions were used to calculate non-equilibrium diffusion behavior. Similarly, a thermodynamic description of a material system can be used as input to solidification models. [15]

2.3.1 Thermodynamic Software Packages

- JMatPro by Sente Software
  - Uses vast thermodynamic and kinetic databases to calculate stable and metastable phase equilibrium phases and resulting mechanical, chemical, physical, and thermo-physical properties
  - Calculates equilibrium and non-equilibrium solidification and phase transformation behavior

- Thermo-Calc by Thermo-Calc Software
  - Uses the thermodynamic principle of minimization of Gibbs Free Energy to create equilibrium isotherms and isopleths for multicomponent materials systems
  - Databases are developed using the CALPHAD (Calculation of Phase Diagram) approach

- Pandat by Computherm LLC
  - Utilizes the CALPHAD approach to develop multicomponent phase diagrams

2.4 KINETIC MODELING

JMatPro is the only software package utilized that easily considers both thermodynamics and kinetics. Thermo-Calc performs strictly equilibrium calculations, but another software package by Thermo-Calc software is also available, TC-PRISMA, which accounts for kinetics. Thermo-Calc output data can be manually entered as input into the TC-PRISMA software.

With the aid of faster computer power, modeling in general has become more common. This is particularly true for kinetic models of multicomponent systems, for example for alloys with upwards of nine elements. Computing time increases significantly with the addition of each element, resulting in lengthy calculations. Numerous papers have been written recently that exploit the relatively new capability of kinetic models, particularly with the user-friendly JMatPro package [16-20]. Of the kinetic software packages, JMatPro requires the fewest user-inputted parameters, making it an effective tool when experimental parameters are not available.

2.4.1 Kinetic Software Packages

- TC-PRISMA by Thermo-Calc Software AB and QuesTek Innovations LLC
  - Builds on the thermodynamic databases and calculations of Thermo-Calc by considering diffusion and kinetic factors to simulate concurrent nucleation, growth, and coarsening
  - Employs Langer-Shwartz theory and Kampmann-Wagner numerical approaches for multicomponent and multi-phase systems

- JMatPro by Sente Software
  - See Section 2.3.1

2.5 SOLIDIFICATION MODELING LITERATURE REVIEW

2.5.1 Simplified Cooling Rate Model

Since this research concentrated on material in the form of atomized powder to be used in the cold spray process, solidification of powder particles was focused on, rather than general solidification techniques, such as casting or wrought alloys. Investigation into the source of powders sprayed at the Army Research

Laboratory revealed formation of the powders via the gas atomization process. Cooling rates achieved during powder atomization can reach upwards of 10^7 °C/sec. This is several orders of magnitude faster than other solidification processes, and therefore needs to be treated differently.

While there are numerous solidification models and theories, a small percentage focused on solidification of tiny quantities at rapid cooling rates; ideal to model the gas atomization process. [21-27]

A simple heat transfer model which represents powder particle solidification during the gas atomization process was presented by He et al. [21] The theory leading up to this final equation began with a common heat balance of a molten powder particle. The heat balance equation is given,

$$-V\rho C_p \frac{dT_d}{dt} = hA_s\left(T_d - T_g\right) + \sigma_{SB}\varepsilon\left(T_d^4 - T_f^4\right) \quad (1)$$

where V is the volume of the droplet [m^3], ρ is the droplet density [kg/m3], C_p is the specific heat of the droplet [J/(kg·K)], T_d is the droplet temperature [K], t is time [s], h is the heat transfer coefficient [W/(m^2·K)], A_s is the surface area of the droplet [m^2], and T_g is the gas atomizing temperature [K], σ_{SB} is the Stefan-Boltzmann constant [W/(m^2·K^4)], and ε is emissivity.

Assuming spherical droplets with diameter d [m] and negligible heat loss due to radiational effects, Equation 1 became,

$$\frac{dT_d}{dt} = -\frac{hA_s}{V\rho C_p}\left(T_d - T_g\right) = -\frac{6h}{\rho C_p \boldsymbol{d}}\left(T_d - T_g\right) \quad (2)$$

It was evident from this equation that the droplet cooling rate, dT_d/dt, was dependent on the density and specific heat of the molten droplet. This would show variation in cooling rates between the various alloys used. Also, cooling rate is inversely proportional to droplet size – large droplets cool more slowly than smaller droplets. Finally, the heat transfer coefficient and the temperature difference between the atomizing gas and the droplet temperature comprise a large portion of the rate at which heat is removed from the particle.

The heat transfer coefficients were approximated using the relationship developed by Szekly, [28]

$$h = \frac{k_g}{d}\left[2.0 + 0.6\sqrt{Re}\ \sqrt[3]{\mathrm{Pr}}\right] \quad (3)$$

where k_g is the thermal conductivity of the gas [W/(m·K)], Re and Pr are the unitless Reynolds and Prandtl numbers, respectively.

According the Estrada [29], the Reynolds number was approximated by,

$$Re = \frac{U\rho_g d}{\mu_g} \quad (4)$$

where U was the relative velocity between the gas and the molten droplets [m/s] and ρ_g [and μ_g were the density kg/m^3] and kinematic viscosity [m^2/s] of the gas, respectively.

Substituting Equation 4 into Equation 3, then Equation 3 into Equation 2 yielded,

$$\left|\frac{dT_d}{dt}\right| = \frac{6}{\rho C_p}(T_d - T_g)\left[\frac{2.0k_g}{d^2} + 0.6\frac{k_g}{d^2}\sqrt{\frac{\rho_g U}{\mu_g d}}\sqrt[3]{Pr}\right] \quad (5)$$

The approximation that the relative velocity between the gas and the droplets approaches zero during gas atomization by Zheng et al. [30] greatly simplified this equation. This lead to the simplified, final droplet cooling rate equation,

$$\left|\frac{dT_d}{dt}\right| = \frac{12}{\rho C_p}(T_d - T_g)\frac{k_g}{d^2} \quad (6)$$

From this simple cooling rate equation it was noted that the rate at which the powder particle cooled is dependent on the intrinsic thermophysical properties of the melt (ρ and C_p), as well as the gas (k_g). While these properties cannot be changed for a given alloy, the other variables may be altered – temperature of the gas used as well as the droplet size (function of gas velocity, nozzle size and shape, etc.). As before, cooling rate is inversely proportional to the squared particle diameter.

3 COMMERCIAL SOFTWARE PACKAGES: THEORY

The basis on which all of the software packages utilized in this work (Thermo-Calc, JMatPro, Pandat, and TC-PRISMA) is the CALPHAD approach. As discussed earlier in sections 2.3 and 2.4, CALPHAD is an acronym for CALculation of PHAse Diagrams. Prior to using the CALPHAD approach, phase diagrams were determined experimentally, typically for binary, but occasionally ternary, alloys. While these proved to be accurate, they were hardly useful in "real world" applications where multicomponent alloys were more commonly used. Multicomponent CALPHAD predictions are based on theoretical and empirically derived data extrapolated from binary and ternary systems.

Simply put, the CALPHAD approach utilizes the minimization of a system's free energy to determine a universal equilibrium. Occasionally, software may mistake a local equilibrium for a universal equilibrium. Software parameters can be adjusted to decrease the likelihood of this occurrence, often only at the sacrifice of processing time. In order to calculate the free energy of a system, thermodynamic values of the various binary alloy systems must be determined experimentally.

3.1 EXPERIMENTAL DATABASE DEVELOPMENT

The calorimetric method is used to experimentally measure many of the necessary parameters used in CALPHAD predictions. Adiabatic calorimeters are used to measure the heat absorbed or emitted by a sample when heated continuously in an adiabatic environment. Heat capacities and resulting enthalpies of transformation can be measured using this method.

An additional method for measuring enthalpies of transformation include differential scanning calorimetry (DSC) and differential thermal analysis (DTA). DSC measures the heat absorbed or emitted during a phase transformation or reaction. DTA uses a similar method but rather than heating at a constant rate, a reference material is used to set the rate, and the difference in heat required to maintain identical temperatures Is used to determine the enthalpy.[31]

Activities of components are often calculated using gas phase equilibria techniques. They utilize the relationship between activity of a component i, a_i, with the vapor pressure of the component i, p_i, and equilibrium vapor pressure of i, $p^0{}_i$,

$$a_i = \frac{p_i}{p_i^0} \tag{7}$$

This method is popular due to the simple measurement of vapor pressure.

Partial Gibbs energies can be calculated by creating electrochemical cells of binary and ternary systems to and measure resulting electromotive forces (EMF).

Databases of these parameters are developed by various software companies and are typically the most costly part of a software package due to the extensive research that is required to build a complete database. These databases allow for the calculation of theoretical phase diagrams for binary, ternary, and higher order multicomponent systems. In order to improve on these calculations, experimental binary and ternary diagrams are created. Calorimetric methods and classic metallography are typically used for these experiments. Since calorimetric methods might better represent a metastable equilibrium condition, metallography, such as optical and scanning electron microscopy, as well as x-ray diffraction are also used.

These compiled databases and experiments are one explanation for the variation in outputted results by the various software packages.

3.2 Fundamental Equations

The Gibbs free energy of a system is calculated using the free energy values of each phase. Phases are either solutions or stoichiometric compounds. The two equations for these types are given below, respectively,

$$G = G^o + G_{mix}^{ideal} + G_{mix}^{XS} \tag{8}$$

$$G_{|T,P|} = H_{|T,P|} - TS_{|T,P|} \tag{9}$$

Where G^0 is the free energy contribution of the pure components of the phase, G^{ideal}_{mix} is the ideal mixing energy contribution, and G^{XS}_{mix} is the Gibbs excess energy of mixing (contribution from non-ideal interactions between components), and $H_{|T,P|}$ and $S_{|T,P|}$ are the enthalpy and entropy as a function of temperature and pressure, respectively.

Various models are used by each software package to account for the various types of solutions – simple mixtures, dilute solutions, ideal solutions, regular solutions, etc. Standard thermodynamic principles are applied to each situation. More information regarding the specific thermodynamics involved in these calculations may be found in Section 5.3 of the book, *CALPHAD – A Comprehensive Guide [31]*.

3.3 Extrapolation to Multi-component Systems

Extrapolation of binary system thermodynamic properties are based on the summation of excess parameters utilizing various geometrical weightings of the mole fractions of the components [32]. Excess energy of a multi-component system, ternary for simplicity, utilized by at least the JMatPro software is given by the Muggianu equation [33],

$$G_{mix}^{XS} = x_A x_B\{L_{AB}^0 + L_{AB}^1(x_A - x_B)\} + x_B x_C\{L_{BC}^0 + L_{BC}^1(x_B - x_C)\} + x_A x_C\{L_{AC}^0 + L_{AC}^1(x_A - x_C)\} \tag{10}$$

Where L is an excess ternary interaction parameter ($G_{ijk} = x_i x_j x_k L_{ijk}$), and x_i are the mole fractions of the components. Interaction terms are neglected for greater than three components since they have proven to be of little significant value to the models. Graphically, this can be represented by Figure 5. Note that the line connecting the multi-component system composition, represented by the blue dot, is perpendicular to the compositions on the three binary phase diagrams, represented by the tan dots. Other models have been used in the past and have different geometrical constructions.

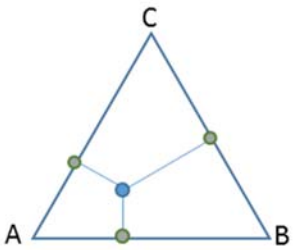

Figure 5. Geometrical construction of the Muggianu model for free energy extrapolation. The blue dot in the ternary diagram represents the composition of the multi-component system. The tan dots represent the composition on each respective binary system that is used in the calculations.

3.4 COMPUTATIONAL MODELING

The CALPHAD method has a simple goal: to minimize the Gibbs free energy of the system, *G*. The equally simple rule of mixtures can be applied to calculate this total,

$$G = \sum_i n_i \overline{G_i} \tag{11}$$

where n_i is the amount of component *i* and $\overline{G_i}$ is the chemical potential of component *i* represented by,

$$\overline{G_i} = \overline{G_i^o} + RT \ln a_i \tag{12}$$

where $\overline{G_i^o}$ and a_i are the standard chemical potential and activity of species *i.* Considering the standard mass balance,

$$\sum_i a_{ij} x_i = n_j \quad (j = 1,2 \ldots m) \tag{13}$$

Where a_{ij} is the number of atoms of element *j* in species *i*, x_i is the number of moles in species *i*, and n_j is the total number of moles of *j* in the system.

In 1957 Dantzig et al developed linear programming approach using the equation,

$$\frac{G}{RT} = \sum_i x_i \left(\frac{\overline{G_i^o}}{RT}\right) + x_{total} \sum \left(\frac{x_i}{x_{total}}\right) \ln \left(\frac{x_i}{x_{total}}\right) \tag{14}$$

where $x_{total} = \sum_i x_i$.

Equation 14 yields the Gibbs energy of the system, *G*, to be calculated as a linear function of $\left(\frac{x_i}{x_{total}}\right) \ln \left(\frac{x_i}{x_{total}}\right)$. The minimal value of G is calculated iteratively. This model was the basis for the software packages used in this research.

Equation 14 is used to calculate a point equilibrium, that is, a defined composition, temperature, system size, and pressure, with no degrees of freedom available. It is often more useful to determine the equilibrium state of a system varying one or two of those properties, resulting in a line or map calculation, respectively. Figure 10 shows an example of a step calculation where the one degree of freedom is the temperature. Figure 9 is an example of a map calculation, where the two degrees of freedom are

temperature and composition of one element. A map calculation is more commonly referred to as a phase diagram or isopleth. A step diagram changes one property incrementally from a minimum to a maximum and calculates the free energy at each step.

In the phase diagrams, the temperature and composition (or pressure and composition) are approached as a series of step calculation, which are in turn a series of point calculations. Phase diagrams are calculated by sequentially incrementing the temperature (or pressure) and composition and recognizing boundaries where one phase varies from one side of the boundary to the other. Each software package has its own proprietary method for determining the boundary conditions within a user-defined tolerance.

An additional attempt at improving calculations, these software packages incorporate extensive experimental data for binary and ternary systems. Each package has its own error minimization algorithms used to combine experimental with theoretical data. Two of the most common optimization programs are PARROT and Lukas and make up the brains of two of the most common commercially available CALPHAD-based software packages, Thermo-Calc and JMatPro, respectively.

3.5 KINETIC CONSIDERATION

Kinetic additions to CALPHAD software packages were initially added by manually suspending stable phases to leave metastable phases. Since then, improvements have been made to utilize diffusion, enthalpy of formation, and other parameters to make more robust models. Gulliver (1922) and Scheil (1942) models are both utilized in commercially available software, and has proven to be extremely accurate for conventional cooling rates when compared to experimental values [31], particularly for aluminum alloys. The Scheil model assumes that solute diffusion in the solid phases is negligible and diffusion in the liquid is fast enough to assume complete diffusion. Since kinetic considerations for micro-segregation and back-diffusion are not considered, this is actually a true kinetic model.

3.5.1 Thermo-Calc's Kinetic Consideration

The software package by Thermo-Calc Software, TC-PRISMA, is based on Langer-Schwartz theory and Kampmann-Wagner numerical method. This allows for the simultaneous solution of concurrent nucleation, growth, and coarsening of dispersed phases. For more of this theory, see D. Belsito's Ph.D. qualifying exam review paper, [34].

3.5.2 JMatPro-Specific

3.5.2.1 Materials Properties Predictions

JMatPro software also combines a materials property database to predict materials properties of the alloys for point and step calculations for stable and metastable phases. Properties have been measured experimentally for various precipitates in each material type (i.e. Al, Ti, steels, etc.) for various shaped particles. These data include molar volume, thermal conductivity, Young's modulus, and Poisson's ratio and for multicomponent alloys are calculated using basic pair-wise models. While specific details of the algorithms used are proprietary, they are similar to the thermodynamic excess functions used in multicomponent alloys. Once the individual phase properties are defined, these data are called upon by the software to predict properties of multicomponent alloys using proprietary mixture models. Extensive experimental verification has been reported [17].

Additional Materials properties can be calculated using known relationships between certain properties (e.g. electrical and thermal conductivity) without the need for additional databases. Other properties that this pertains to include

- Volume, density and expansion coefficient
- Young's, bulk, and shear moduli
- Poisson's ratio, thermal conductivity, and diffusivity
- Electrical conductivity and resistivity

Examples of theory of materials properties not utilized in this particular work include calculation of ultimate tensile stress and hardness from the Hall-Petch relationship, consideration of grain coarsening by Ostwald Ripening, and Jominy Hardenability in steels by continuous-cooling transformation curve (CCT) calculations.

3.5.2.2 Thermodynamic Models

Time-temperature-transformation (TTT) and CCT diagrams are also calculated in JMatPro using the Johnson-Mehl-Avrami equation as a foundation. Since the original work was for spherical particles, additional changes have been applied to account for the effect of non-spherical precipitates. Not only are the additional model equations needed, work needs to be done to assess the nucleation shape and characteristics for each precipitate as well as experimental comparison.

Strengthening mechanisms by the various phases present are incorporated by solid solution strengthening as well as precipitation hardening. If the material is not recognized, semi-empirical approaches are used instead of the physical models [35].

3.5.2.3 Solidification Modeling in JMatPro

Solidification modeling in JMatPro allows for the calculation of the cooling curve during solidification based on the fraction of solidified material calculated with the Sheil calculation, given the initial cooling rate. The initial cooling rate is the rate at which the material is cooling before any solid forms in the liquid. This is nearly a constant rate.

Two heat-related processes occurring during solidification are heat loss from the sample to the surroundings and recalescence. JMatPro uses the following equation to calculate heat loss to the surrounding,

$$Q_{ext} = A_1 C_p V_c \tag{15}$$

where A_1 is a material constant and may be dependent on cooling rate, C_p is the specific heat neglecting phase transformations, and V_c is the constant cooling rate of the liquid phase before any solidification occurs. Since none of the parameters on the right side of the equation change with temperature, Q_{ext} is constant.

The total heat extracted after time t is given by,

$$H_{ext} = Q_{ext} t \tag{16}$$

The other heat-related process, recalescence, is the latent heat of transformation (liquid to solid) and can be approximated up to a critical temperature from,

$$H_{rel} = f_s(T)L \tag{17}$$

where $f_s(T)$ is the fraction solid formed when cooled to temperature, T. L is the latent heat of transformation.

During solidification, $H_{rel}(T) = H_{ext}$ df, therefore

$$Q_{ext}t = f_s(T)L \tag{18}$$

This allows for the calculation of the time-temperature cooling curve.

Since the assumption of a constant initial cooling rate does not hold true for many alloys during the entire range of solidification, appropriate adjustments have been made, particularly for aluminum alloys. With this consideration, experimental data agree well with the predicted curves [35].

Dendrite arm spacing (DAS & λ) is another characteristic predicted by JMatPro. Extensive research was performed to build an accurate model. The relationship between the velocity of the dendrite tip, thermal gradient, and DAS is given by,

$$\lambda = A(GR)^{-n} \tag{19}$$

where G is the thermal gradient at the liquid-solid interface, R is the velocity at the dendrite tip, A is an alloy-dependent parameter, and n is an exponent, assumed to equal $1/3$. This relationship does consider dendritic arm coarsening during solidification, resulting in the disappearance of thin branches.

Due to the difficulty in measuring dendrite tip velocity, the thermal gradient and tip velocity in Equation 19 were replaced by cooling rate, V_c, which yields,

$$\lambda = A(V_c)^{-n} \tag{20}$$

The constant, A, can be defined for any system by,

$$A = \frac{A_o}{\sum_i c_i x_i + \sum_{i,j} c_{ij} x_i x_j} \tag{21}$$

where c_i, c_{ij} are the corresponding coefficients and A_o is a constant, independent of alloy chemistry.

Combining Equations 20 and 21 yield a function for dendrite arm spacing as a function of cooling rate and coefficients. The coefficients are found by empirically fitting curves against experimental data.

A final note regarding solidification models in JMatPro is considering the cooling rate definition. Many calculations in the software are functions of the cooling rate. JMatPro uses the cooling rate of the liquid before which any solid forms as the only cooling rate of the system. They choose this because the latent heat released during recalescence changes continuously and is very different from the beginning to the end of the process. The cooling rate before solidification represents the ability of the cooling media to extract heat. Also, this rate can be controlled, so the model could be run to determine ideal cooling rates for desired outcomes.

3.5.2.4 Strengthening Mechanisms

After solidification models determine final microstructure, the strength contributions from resulting phases formed can be quantified. Yield strength and tensile strength can be calculated based on the contributions of solid solution strengthening and precipitation hardening from intermetallics.

Three types of strengthening mechanisms are considered: solid solution strengthening, precipitation hardening, and dendrite arm spacing size effect. The phases that contribute to these mechanisms are primary phases, eutectics, and intermetallics.

Intermetallic phases (dendritic, hypoeutectic, etc.) are known from the solidification calculations. Particle size is considered; particles over a critical size are not contributing to the overall material strength and are therefore neglected. For primary Al phase, solid solution strengthening is first calculated, then the size effect of DAS is added. Total strength, σ_o, from solid solution strengthening for one phase is calculated from,

$$\sigma_o = \sum_i x_i \sigma_i^o + \sum_i \sum_j x_i x_j \Omega_{ij} + \cdots \tag{22}$$

where is σ_i^o is the strength of pure element *i*, x_i and x_j are the atomic fractions of elements *i* and *j*, respectively, and Ω_{ij} are associated with the solute interactions.

The addition of strengthening due to dendrite arm spacing is calculated from,

$$\sigma_{den} = \sigma_o + k_{den}\lambda^{-0.5} \tag{23}$$

where σ_{den} and k_{den} are the flow stress and Hall-Petch coefficient for the dendritic phase, respectively. Databases containing these values are present in the software and were developed experimentally.

If a eutectic phase is present, its contribution to the strength is calculated,

$$\sigma_{eut} = (f_A\sigma_A + f_B\sigma_B)/f_{eut} + f_{eut}\lambda^{-0.5} \tag{24}$$

where *f* is the fraction of elements A and B in the A-B eutectic, and σ_A and σ_B are the strength of A and B in the A-B eutectic. σ_A *is effectively* σ_o in Equation 22, $f_{eut} = f_A + f_B$, *and* k_{eut} is the Hall-Petch coefficient. From this equation it is evident the impact that dendrite arm spacing has on strength.

In JMatPro, precipitates are assumed unable to shear. Their strength contribution is modeled by Orowan looping mechanism, updated by Ashby to create the Ashby-Orowan relationship, yielding an equation for the strength contribution by the precipitates, σ_{ppt},

$$\sigma_{ppt} = 0.84M\left(\frac{1.2Gb}{2\pi L}\right) ln\frac{r}{b} \tag{25}$$

where *M* is the Taylor factor (typically close to 3), *r* is the particle radius, *b* is the burger's vector, *G* is the shear modulus, *r* is the particle radius, and *L* is the inter-particle spacing, given by,

$$L = \left(1.23\sqrt{\frac{2\pi}{3f_{ppt}}} - 2\sqrt{\frac{2}{3}}\right)r \tag{26}$$

assuming spherical particles. Since measuring particle sizes during solidification is difficult, a relationship between cooling rate (inversely proportional to time) and particle size by,

$$r = r_0 * V_c^{-1/3} \tag{27}$$

Where the only unknown is r_o which is independent of alloy chemistry and is determined by curve fitting experimental data.

Combining the previous strength equations, the overall yield strength of a casting alloy can be calculated,

$$\sigma_y = f_p\sigma_p + \sum_i f_i\sigma_i + \sigma_{ppt} \tag{28}$$

where $f_p$and σ_p are the fraction and strength of the primary phase, respectively, and in many cases, a dendritic phase. $f_i$and σ_{pi} are correspond to the various types of eutectics. This model showed good agreement with experimental work [35].

Quantitative relationships between yield stress (Equation 28), tensile stress, and hardness allow the latter two properties to be calculated based on the physical systems set up in the previous paragraphs. The basis of these calculations is the assumption of the relationship between stress (σ) and strain (ε),

$$\sigma = B\varepsilon^m \tag{29}$$

where *B* is a constant and *m* is the work-hardening coefficient.

The average pressure under a hardness indenter of known geometry can be determined; this allows for the derivation of equations relating hardness *Hv*, yield stress σ_y, and tensile stress σ_t,

$$Hv = C\sigma_y(40^m) \tag{30}$$

and

$$\sigma_t = \sigma_y(40)^m(1-m)(\tfrac{12.5m}{1-m})^m \tag{31}$$

where C is between 2.9 and 3.3 (good agreement with theoretical value of 3). Also,

$$m = a\exp(b\sigma_y) \tag{32}$$

where *a* and *b* are alloy dependent and are fitted empirically.

Again, good agreement between values predicted using these equations and experimental data were reported [35].

4 MODEL DEVELOPMENT

4.1 MODELING OVERVIEW

Initially in this research, Pandat software was used to create unique isopleths and isotherms for the individual alloys used in the cold spray process. This allowed for the most thermodynamically stable equilibrium phases to be predicted.

Subsequently, JMatPro and Thermo-Calc software were utilized to predict stable and metastable phases present in various alloys, including both those that were currently cold sprayed as well alloys that showed behavior that typically yield favorable results to potentially spray in the future. Chemical composition of the powders were altered to determine which phases would be present with equilibrium and non-equilibrium conditions.

A further model was created using data calculated in JMatPro to predict the impact of various chemical elements on the formation on both beneficial and deleterious phases. This allowed for the quick determination of alternate composition to current alloys, as well as new alloys to be cold sprayed, that again, exhibit behavior that other well spraying alloys have.

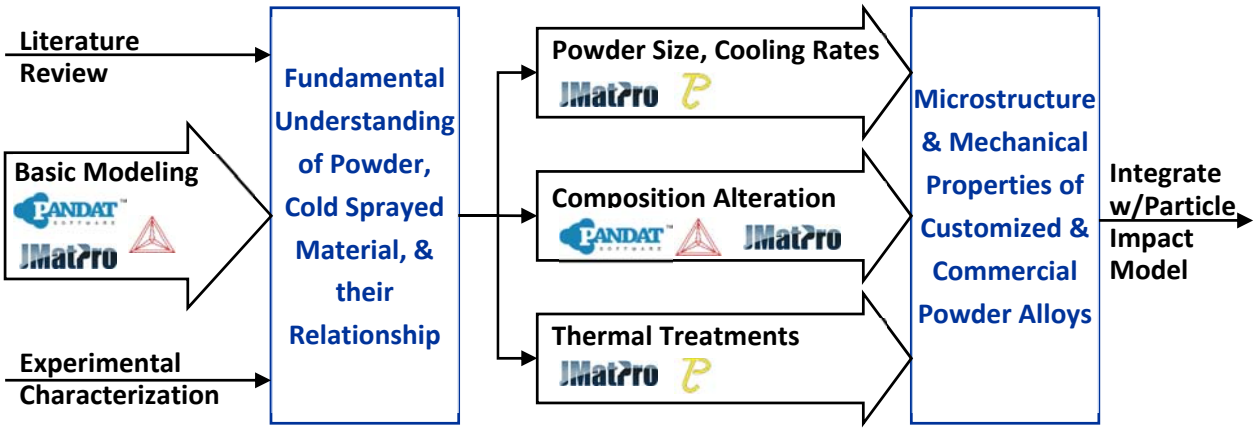

Figure 6. Schematic of the relationship between the models.

TC-PRISMA and JMatPro were used to predict the behavior of multi-component powder alloys used in the cold spray process upon heat treatments. These models were slightly altered to account for the unique behavior of powder. This set of models used were particularly useful in understanding microstructural evolution occurring in the material during the various degassing heat treatments.

JMatPro was used to further calculate solidification and phase transformation behavior, which was utilized in the modeling of the powders to be cold sprayed. A mechanical property model was developed to determine the final microstructure and properties of the powder. These properties will be integrated as input into a powder particle impact during cold spray processing model by L. Bassett, WPI.

A schematic of the relationship between the various models is given in Figure 6.

4.2 THROUGH-PROCESS MODEL

In efforts to predict the behavior of material created with the cold spray process, through-process modeling was utilized to control the entire range of stages in the cold spray process. The inputs to and outputs from these stages will be integrated and optimized to produce a set of material and processing parameters to design high performing materials, optimized for the cold spray process. The five stages are shown in Figure 1. The final outputs are the predicted physical properties of the designed cold spray material.

The first stage, powder production, involved modeling the mechanical properties considering of particle size, composition, microchemistry, microstructure, grain size, and secondary phase size. The second stage, powder processing, involved incorporating any pre-treatments to the powder prior to use in the cold spray process. Since these stages are the primary focus of this paper, they will be discussed in detail in the subsequent sections.

The third and fourth stages in the through-process model both encompass the actual cold spray processing. The third stage, cold spray process parameters, involved the variation of processing parameters such as gas temperature, pressure, and composition, as well as external systems acting during the spraying, such as a laser or other additional heat source. These parameters were optimized for each material being sprayed, as well as for desired consolidated material parameters.

Stage four is the cold spray particle impact simulation. ABAQUS/Explicit axisymmetric and three-dimensional models were used to predict system behavior upon particle impact based on processing parameters, such as impact velocity, particle temperature, and substrate temperature. These parameters will be received from the stage three outputs in addition to outputs of stage 1 – the powder production stage. Behavior aspects at impact include microstructural evolution, heat generation, possible localized melting, and dynamic recrystallization in regions of high plastic deformation.

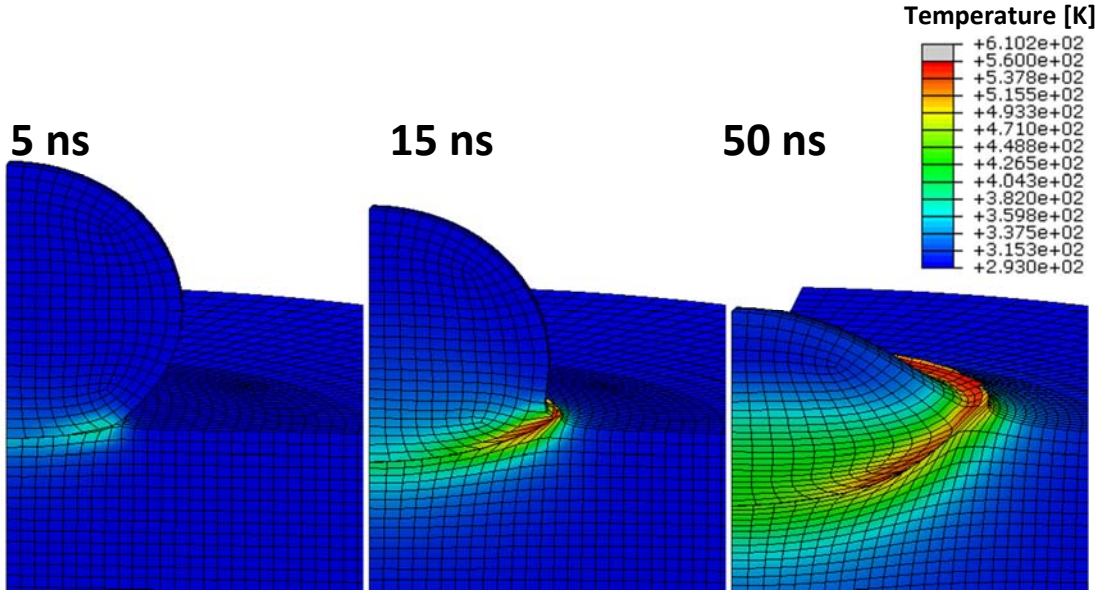

Figure 7. Evolution of shape and temperature of a 50-µm, CP-aluminum powder particle impacting a CP-aluminum substrate at a velocity of 800 m/s at 5 ns, 15 ns, and 50 ns. [36] This is an example of modeling work performed in the cold spray particle impact simulation, stage four.

The final stage of the through-process model is post-spray processing. The least amount of work was done on this section to-date. Potential heat treatment and/or thermochemical surface treatments are processes that may be performed on the as-sprayed material. One initial experiment performed on the as-sprayed Al 6061 alloy at the beginning of this project involved heating cold sprayed Al 6061 samples to temperatures between 100°C and 500°C for times of 0 to 16 minutes. Results are given in Figure 8.

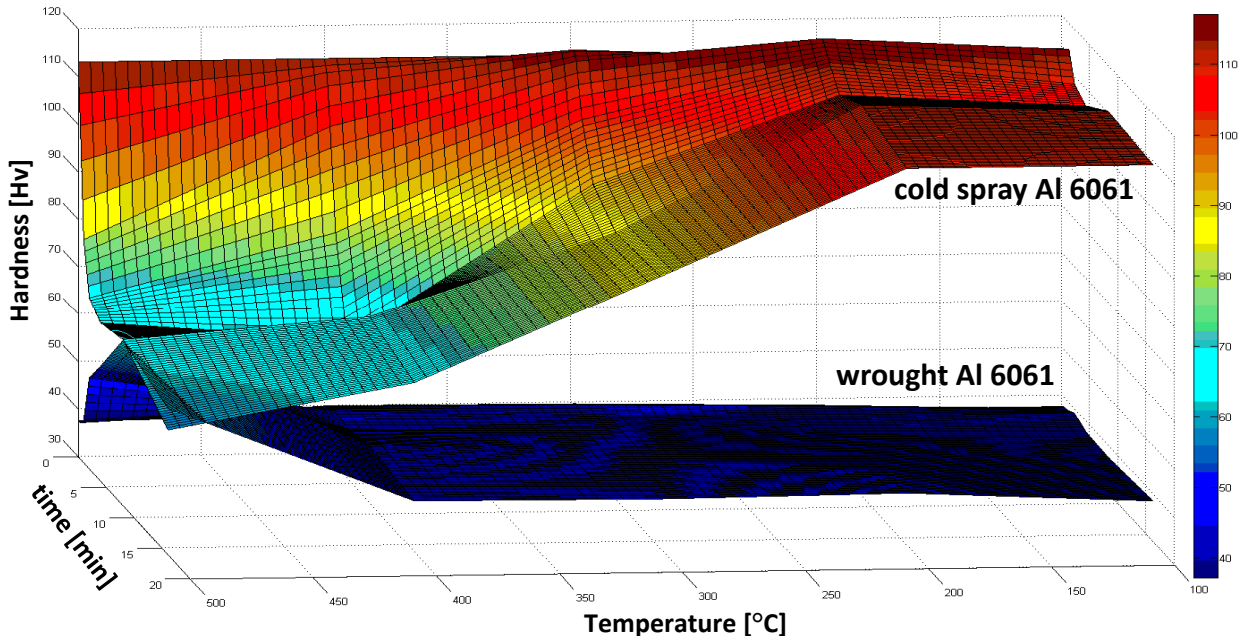

Figure 8. Vickers hardness values of heat treated cold sprayed and wrought Al 6061 alloy samples.

Hardness values for the cold sprayed alloy decreased as time and temperature increased. This exhibited opposite behavior than the traditional wrought alloy. The cold spray process introduced extremely high energy into the consolidated material, which contributed to its unusually high hardness. When the cold spray alloy was heated, these stored compressive stresses are relieved and hardness is decreased. This was the trend observed in the experimental results. For this reason, heat treating processes have since been performed on the powder, prior to undergoing the cold spray process.

Outputs of the through-process model include the overall consolidated material microstructure and resulting mechanical properties. Ideally, outputs from each stage in the through-process model will be inputs to the subsequent stage. Final output material properties will be specified, then the entire model will employ to suggest powder properties, processing parameters, and/or pre/post treatments.

4.3 Thermodynamic Models

In efforts to predict phase equilibria in the powder, and therefore also in the consolidated material, computational thermodynamic principles were used to develop equilibrium isopleths and isotherms. Isopleths show phases present under equilibrium conditions. Minimization of Gibbs free energy is performed to yield the most thermodynamically stable phases. Both Pandat and Thermo-Calc software packages are used for these calculations.

An isopleth of Al 6061 is shown in Figure 9. Due to the large number of equilibrium phases present, the phase names are not shown on the isopleth in this paper. Also, this paper primarily shows the model outputs for Al 6061 as an example of the types of modeling performed. Most analyses were also performed for Al 5083, clean Al 5083, and Al 5056.

The blue dashed vertical line at 1.0 wt% Mg represents the average composition of magnesium in Al 6061. The light blue region between 0.8 wt% Mg and 1.2 wt% Mg represents the allowable range of Mg in Al 6061. It was therefore seen that despite an alloying having a composition within the specification range, several different phases may actually be present, depending on the composition of the particular batch of alloys received. This may account for performance variation between batches of raw materials. Finally, the orange line represents the solubility limit of Mg_2Si in the alloy. This is an example of how these diagrams can be used to visually see how the alteration of chemical composition of an element can produce desired or deleterious secondary phases, and if the alloy exhibits potential for precipitation hardening.

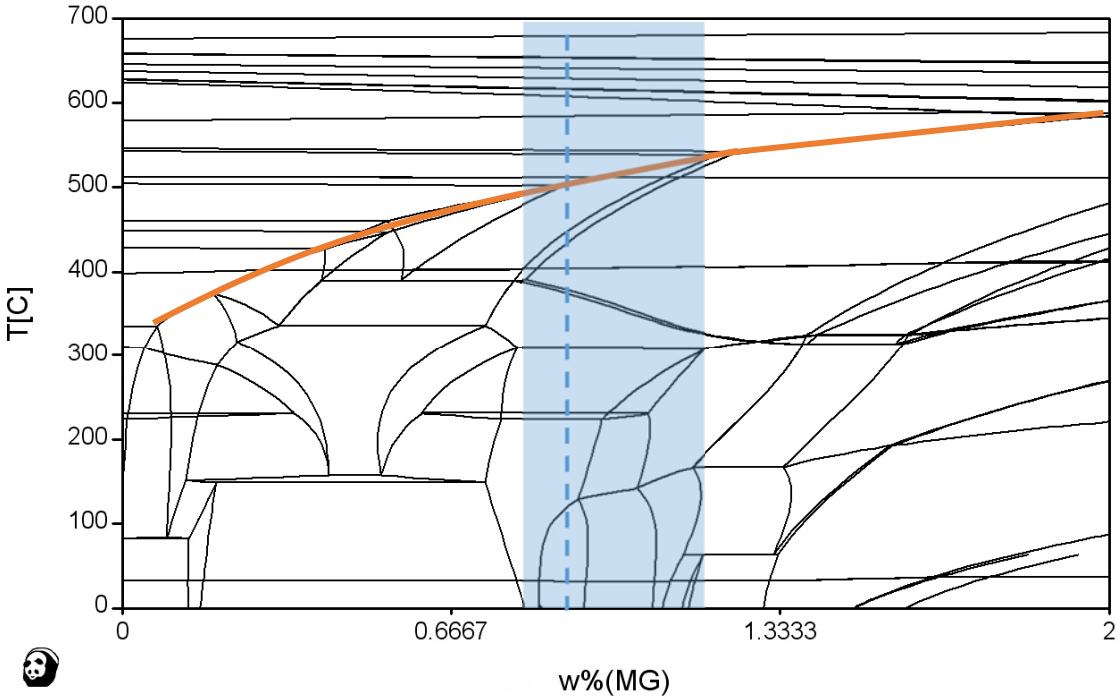

Figure 9. Isopleth of Al 6061 created in Pandat software showing thermodynamically predicted equilibrium phases. The vertical dashed blue line represents the experimentally measured Mg in a batch of Al 6061 powder used in the experiments, 0.9 wt%. The blue shaded area represents the allowable range of Mg in Al 6061, 0.8-1.2wt%. The orange line represents the solubility limit of Mg_2Si in the alloy.

Using similar thermodynamic principles, diagrams showing equilibrium phase fractions as a function of temperature were created, shown in Figure 10 for Al 6061. FCC-Al is the primary phase and is out of viewing range over the majority of the temperature range due to the scale of the diagram. The major secondary phases predicted are Mg_2Si, Al_7Cu_2Fe, and alpha. These predictive models can be verified by

SEM/EDS and TEM/EDS data, and is discussed in Section 6.3, verifying the existence of these phases at room temperature in Al 6061.

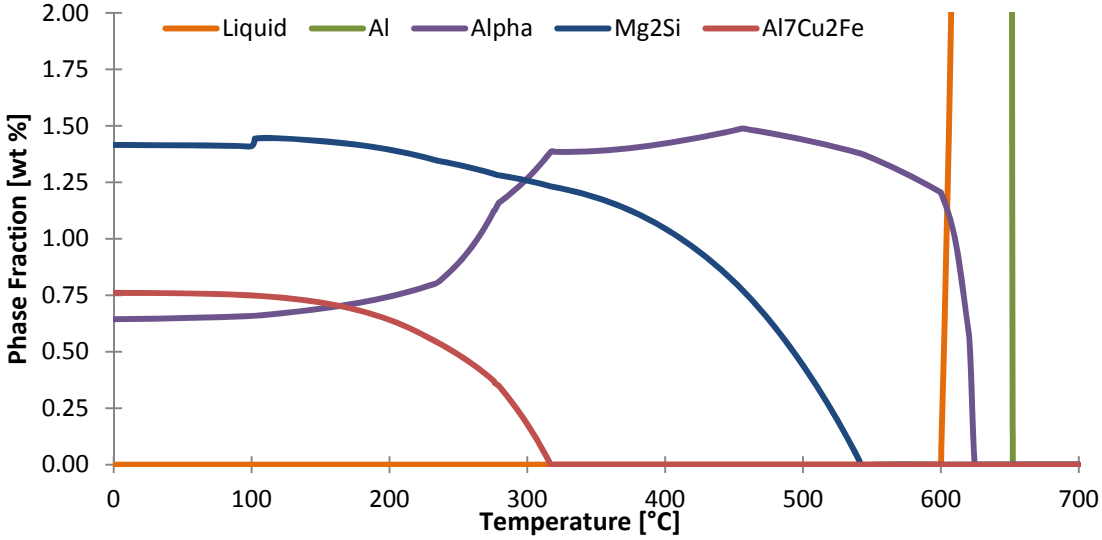

Figure 10. Equilibrium phase fractions in Al 6061 as a function of temperature at the composition given by the blue vertical dashed line from Figure 9 (0.9 wt% Mg). Phases with phase fractions less than 0.25 wt% are not shown.

An additional method utilizing thermodynamic principles to theoretically observe the effect of varying alloying element concentration is shown in Figure 11. These phase variation plots contain data from JMatPro software and will be further discussed in Section 4.6.

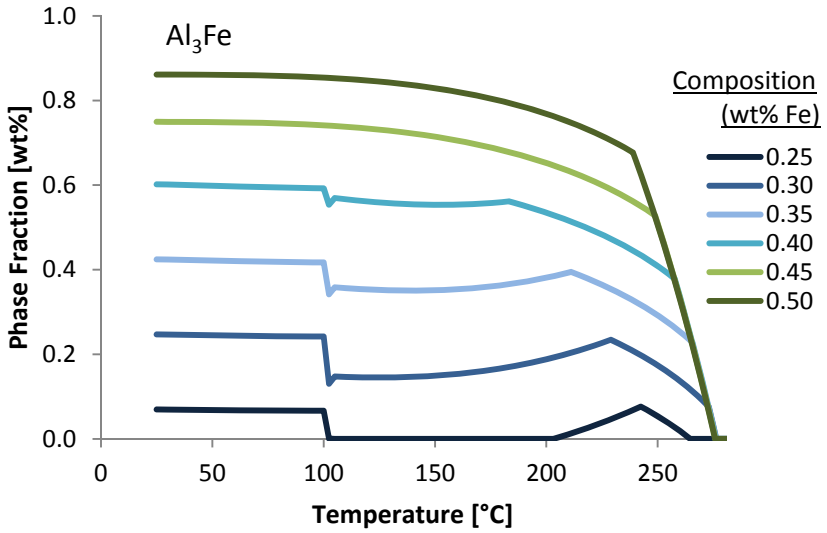

Figure 11. Variation of predicted equilibrium Al_3Fe phase in Al 6061 with a concentration variation of Fe.

4.4 KINETIC MODELS

The thermodynamic models discussed in the previous section are all derived from minimization of the Gibbs free energy of a given system. This is only valid at equilibrium conditions. While equilibrium is a fair assumption to make to acquire an approximate solution, in order to obtain a more accurate sense of a system, kinetic consideration must be given.

Figure 12 shows the isopleth of Al 6061 as a function of magnesium composition at equilibrium. The solid blue line represents the solubility limit of the Mg_2Si phase in Al 6061. The blue shaded region under the line represents the regions on the isopleth where Mg_2Si is present at equilibrium.

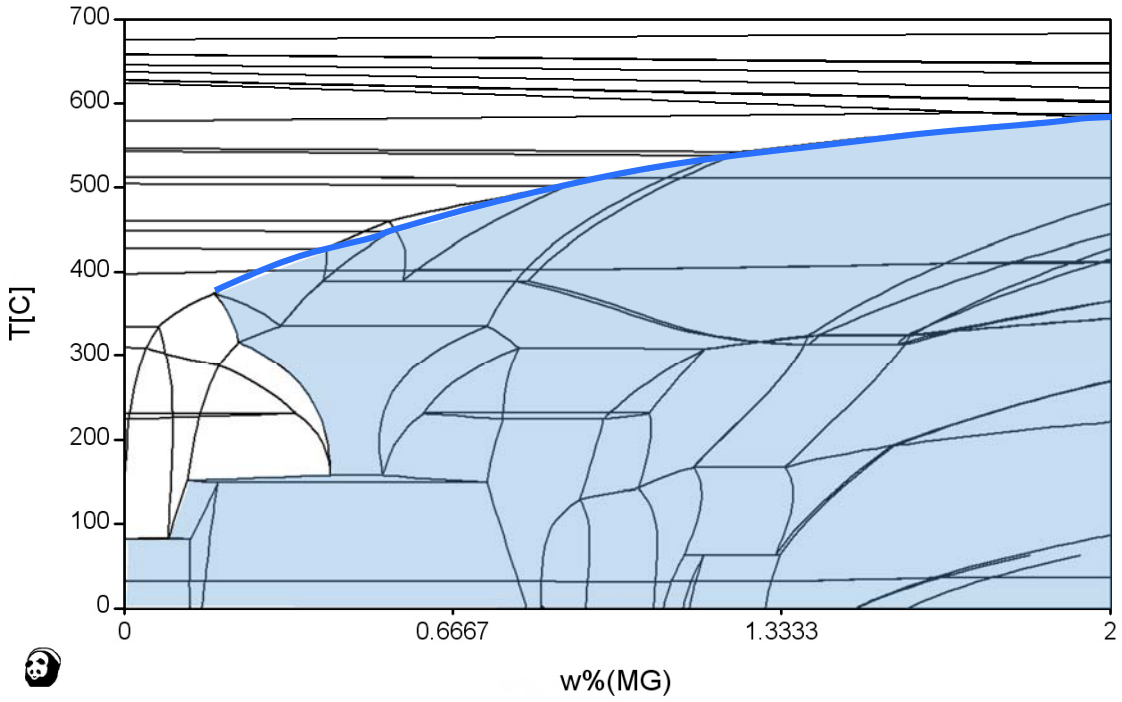

Figure 12. Equilibrium isopleth of Al 6061 with varying concentration of Mg. The solid blue line represents the solubility limit of Mg_2Si in the alloy. The shaded blue region represents the areas where Mg_2Si is present under equilibrium conditions.

This can be contrasted to Figure 13, which considers kinetic effects, such as diffusion behavior, to more accurately predict phases present in a system as a function of time. Figure 13a is a time-temperature-transformation (TTT) diagram for Mg_2Si in Al 6061 created using data from JMatPro. This data can be further manipulated to create plots showing the fraction of Mg_2Si that has formed as a function of time at various temperatures, Figure 13 b-e.

An example of the type of data that can be extracted from these types of predictions compared results from Figure 12 (quantified in Figure 10) and Figure 13. At 200°C at equilibrium there is 1.39 wt% of Mg_2Si. From the TTT diagram, at 200°C it takes 1.0 minute for Mg_2Si to nucleate form. At room temperature, the difference is more exaggerated – it takes nearly four days for Mg_2Si to begin to form.

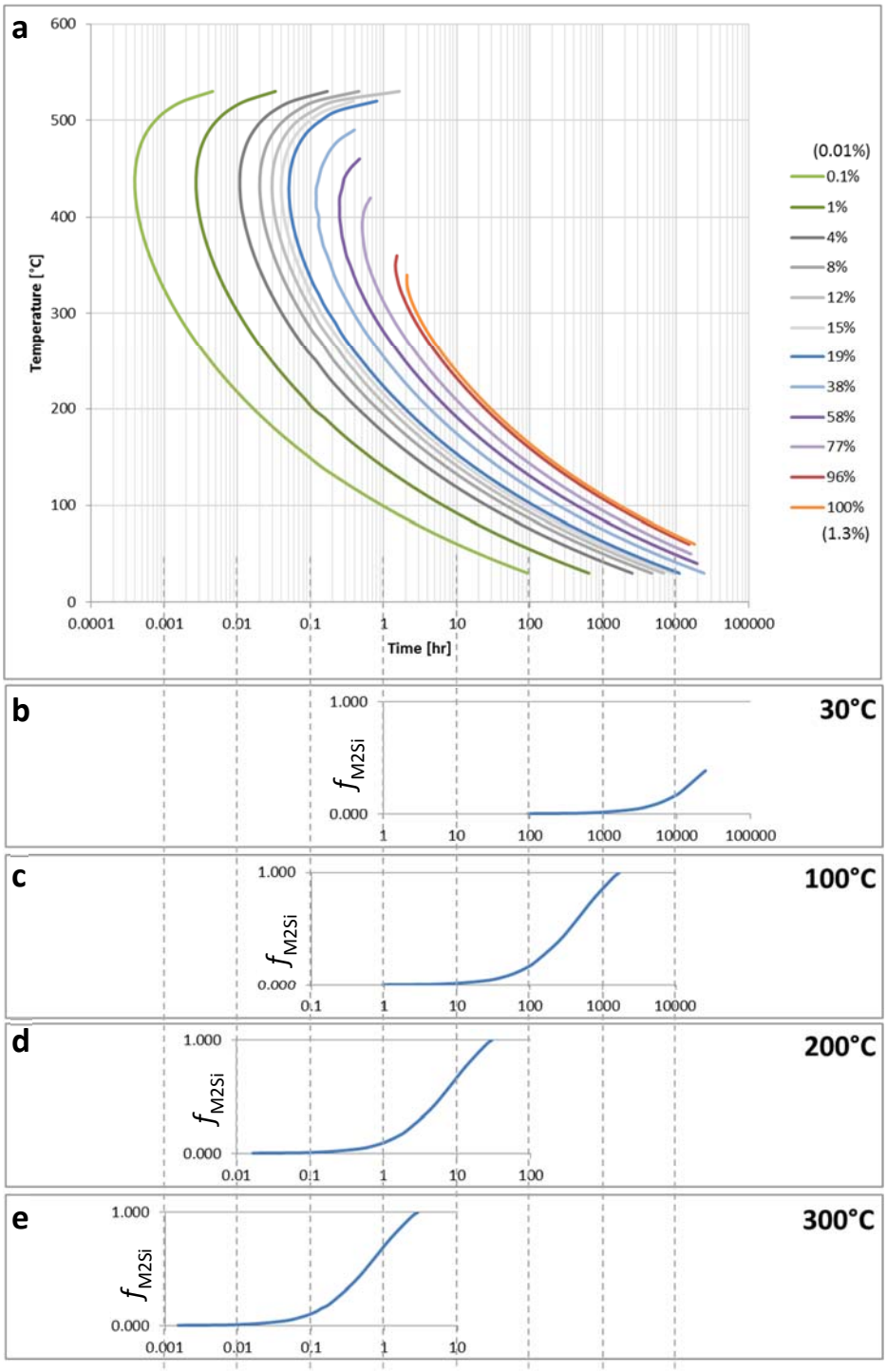

Figure 13a) TTT diagram for the Mg_2Si phase in Al 6061 showing the amount of Mg_2Si phase formed as a function of time and temperature, plotted on a semi-log chart, b-e) fraction of Mg_2Si transformed as a function of time for various temperatures.

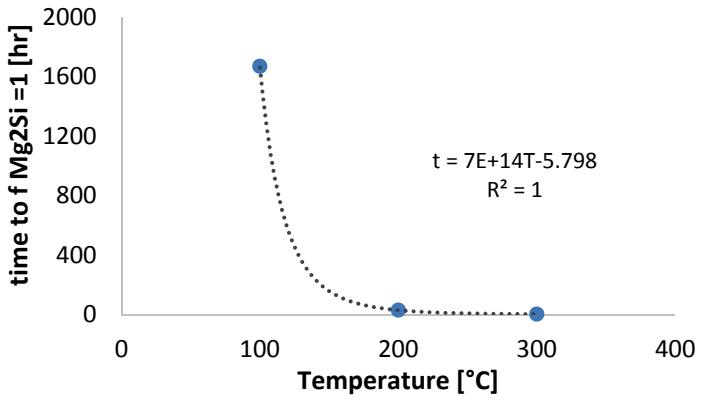

Figure 14. Time for 100% of the Mg_2Si phase to form as a function of temperature. Extrapolating to room temperature, 25°C, results in approximately 602 years before 100% of the Mg_2Si (1.3wt% of the alloy) will form.

It is evident that temperature plays a large role in the type and quantity of phases present. In fact, Figure 14 shows the time it will take for 100% of the possible Mg_2Si phase, which comprises 1.3 wt% of the entire alloy, to form. Between 100°C and 200°C the time for this maximum to be reached decreased by 1641%. The simulations used to create these kinetic diagrams did not run to times long enough to reach 100% Mg_2Si at low temperatures. Data for higher temperatures was plotted in Figure 14a and a power curve was fitted to generate an equation from which the approximate time to reach complete Mg_2Si formation at room temperature was calculated to be 602 years.

This result is not at all evident when observing only the equilibrium isopleth and shows the necessity of kinetic considerations.

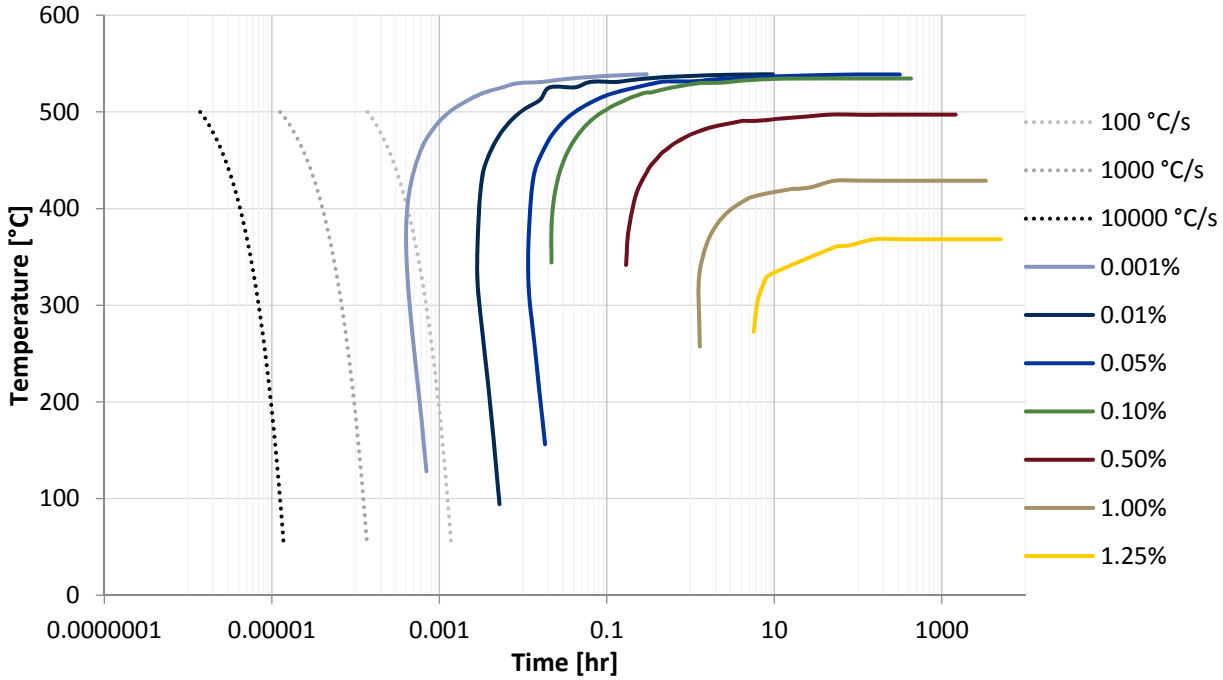

Figure 15. Continuous cooling transformation curves for the formation of Mg_2Si in Al 6061. Powder solidification models for the powders used in this study show cooling rates around $1x10^4$ to $1x10^5$ °C/s, which would result in no Mg_2Si phase forming during solidification.

Models can also be used to calculate the fraction of secondary phases formed during solidification. Figure 15 contains continuous cooling transformation (CCT) curves for the formation of Mg_2Si in Al 6061. Solidification models, discussed in Section 4.5, approximated the cooling rate of most Al 6061 powder particles used in the cold spray process to be $1x10^4$ to $1x10^5$ °C/s. According to the CCT curves for Mg_2Si, no Mg_2Si would form during solidification of these powders. However, cooling rate depends on powder particle size. Larger particles with a slower cooling rate may form additional and more of the secondary phases than smaller particles.

4.4.1 Powder Degassing

The TTT diagrams were specifically useful in modeling a new powder degassing process which the powder underwent before being cold sprayed. During the degassing process, as-received powder particles were heated in an inert environment at temperatures between 150-260°C for times around 24 hours. This was done to remove any oxides and/or hydroxides on the powder particles surface, with the intention that these brittle phases were causing cracking in the consolidated cold sprayed material. This was the method currently designed by the cold spray processing facility operators.

Initial results show that while degassing does reduce the overall material hardness, approximately 15% for an average degassing recipe, the ductility can more than double. Investigation into the material and microstructural changes that the degassing caused was not studied prior to this report; only mechanical measurements were used to understand the changes.

A standard degassing recipe was to heat the powder at 260°C for 24 hours in an inert environment, then transfer the powder directly to the cold spray chamber, preventing any contact with the external

environment. Using Figure 15 and the cooling rates predicted by the solidification models in the next section, no Mg_2Si was predicted to form on solidification. Figure 13 was then used to see if and how much Mg_2Si would form during the degassing process. From this figure at 260°C and 24 hours 100% of the possible Mg_2Si should form, comprising of 1.3%wt of the final alloy composition.

These diagrams can be used to determine the degassing parameters to not only remove deleterious surface phases, but also form beneficial phases in the bulk of the particle. Also, while Mg_2Si is the only phase presented in this work, the analyses was also performed on various secondary phases in the alloys studied and will be presented in a future report.

4.5 SOLIDIFICATION MODELS

As mentioned in the introduction, experimental work that characterized cold spray consolidated material and the powders that comprised them revealed that the majority of phases and microstructure present in the unsprayed powder were the same as those in the consolidated material. Understanding powder formation was therefore of great importance, due to the powder properties' large and direct impact on the final behavior of the consolidated material.

The powders used in the cold spray processing done at the Army Research Laboratory and their affiliates were typically gas atomized. The specific powders used in this work were all formed by this process. In gas atomization, as depicted in Figure 16, a pure metal or alloy melt comes in contact with a high velocity gas stream causing the melt to break up into small particles. The particles solidify as they travel through the atomization chamber, collecting at the bottom as solidified powder particles.

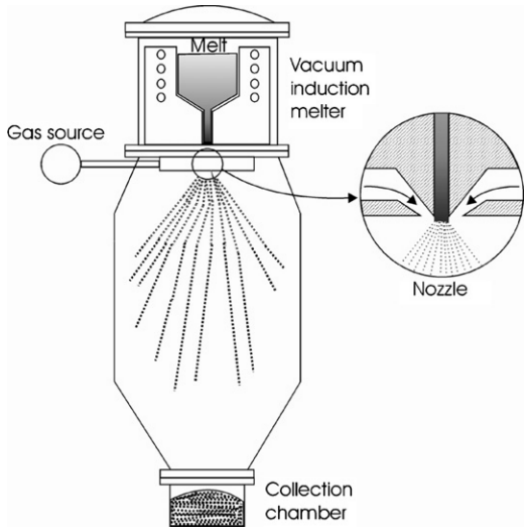

Figure 16. Schematic of the gas atomization process. [37]

The simplified droplet cooling rate model discussed in Section 2.5.1 made general assumptions, such as negligible heat loss due to radiation, to reduce the heat balance, Equation 1, containing numerous particle and gas properties, to the simplified cooling rate formula [21],

$$\left|\frac{dT_d}{dt}\right| = \frac{12}{\rho C_p}\left(T_d - T_g\right)\frac{k_g}{d^2} \tag{33}$$

As schematic depicting the material properties used in Equation 33 is given in Figure 17.

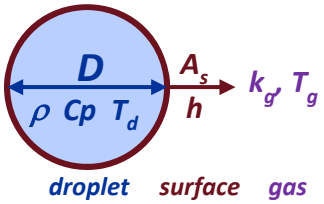

Figure 17. Schematic of the materials properties and parameters use in simplified powder particle solidification model given by Equation 33. A table with these parameters used is given in Table 2.

A table with these thermophysical properties used in a simulation example with argon as the atomizing gas and Al 6061 as the solidifying alloy is given in Table 2. The molten droplet properties were calculated using JMatPro software.

A summary of the simplified powder particle cooling rate model for gas atomization is as follows. Newtonian heat flow is assumed. The heat transfer from the droplet is calculated from forced convention only; radiational cooling is neglected. Heat conduction within the droplet is neglected due to its very small size and low Biot number, typically less than 0.1.

Table 2. Thermophysical properties used in the powder droplet simplified solidification model. Molten droplet properties were calculated using JMatPro software. The thermal conductivity of the argon gas was generated using CES EduPack software.

Thermophysical Properties of Al 6061				
Ar Atomizing Gas		**Molten Droplet**		
T_g	**K_g**	**ρ**	**C_p**	**T_d**
[K]	[W/(mK)]	[kg/m^3]	[J/(kgK)]	[K]
300	1.79E-02	2380	1170	1473

Typical Al 6061 particle size diameters used in cold spray at ARL are between 10 μ and 20 μm. This results in cooling rates between 9.0x10^5 °C/s and 2.2x10^5 °C/s, respectively. These cooling rates were used in conjunction with the kinetic models to obtain likely cooling rates, particularly to determine phases formed at solidification, as well as to determine starting microstructure before the powder undergoes degassing.

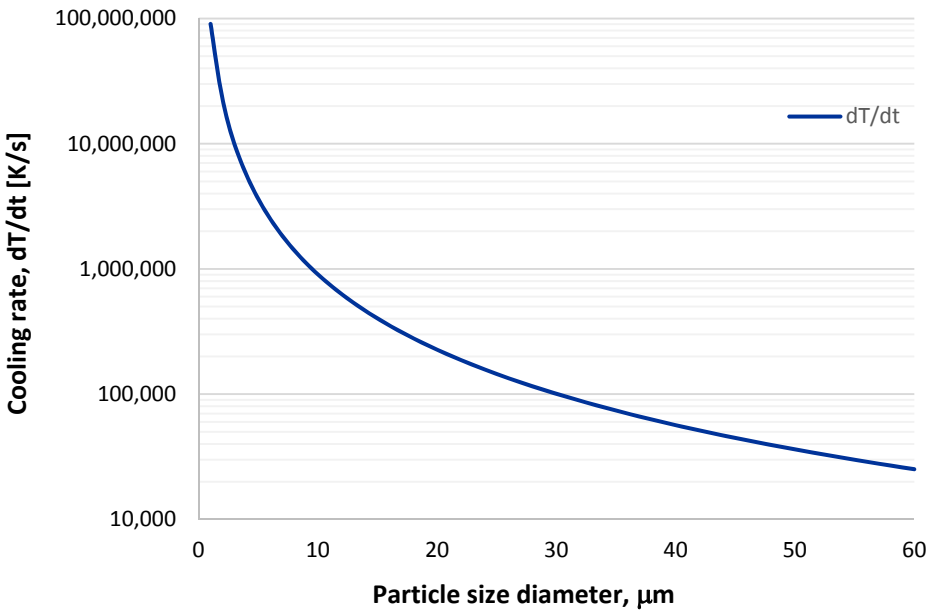

Figure 18. Cooling curve resulting from the simplified solidification model given by Equation 6 for Al 6061 in argon atomizing gas. Parameters used for this prediction are found in Table 2.

4.5.1 Powder Particle Microstructure

The relationship between secondary dendrite arm spacing (SDAS) and cooling rate is given by,

$$\lambda_2 = \lambda_0 \left(\frac{dT_d}{dt}\right)^{-n} \tag{34}$$

Where λ_2 is the secondary dendrite arm spacing [μm], λ_0 [K/s]$^{[n]}$ and n [dimensionless] are alloy system-dependent constants, T is the droplet temperature [C°], and t is time [s], dT_d/dt is therefore the cooling rate of the droplet [°C/s]. SDAS as a function of initial cooling rate data was available from JMatPro. Data for Al 6061 is plotted in Figure 19 and a power law curve was fit to the data to determine the constants λ_2 and n to be 100.99 and 0.33, respectively.

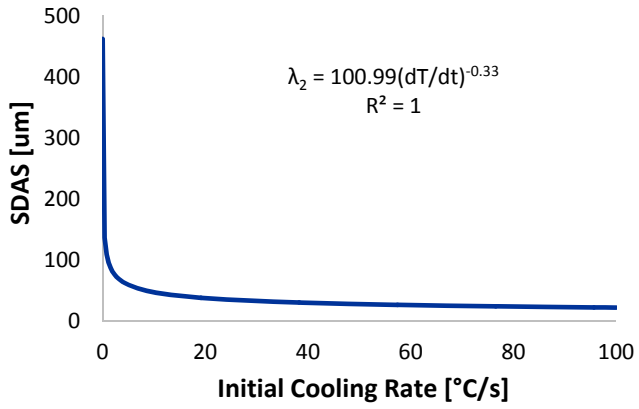

Figure 19. Secondary dendritic arm spacing as a function of initial cooling rate for Al 6061. Data was generated using JMatPro software.

With this data, secondary dendrite arm spacing can be experimentally measured in particles that contain and exhibit dendrites to experimentally calculate cooling rates. Not all particles, however, form dendrites. Particles that solidify at very rapid cooling rates bypass crystallinity entirely, forming amorphous particles. Since particle cooling rate is directly proportional to particle size, with smaller particles cooling more rapidly, the smallest particles are those which form amorphously. Dendrites only form with relatively slow cooling rates, and after the recalescence stage. These are the particles which dendritic arm spacing can be measured, and these "slow" cooling rates can be estimated. Experimental verification of these cooling rate predictions are given in Section 6.3.2.

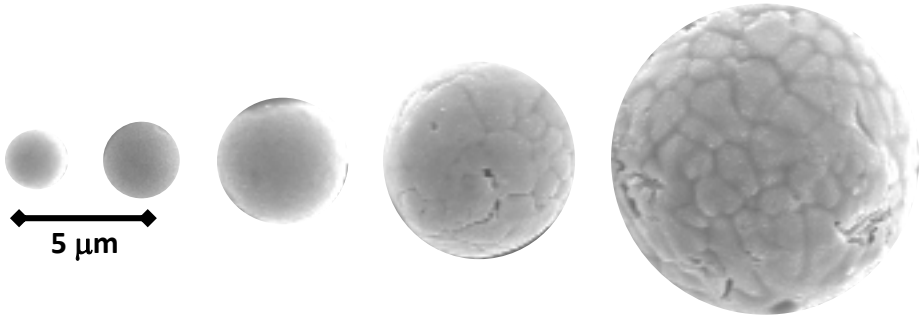

Figure 20. SEM images of Al 6061 powder particles (to scale) showing the varying degree of microstructure as a function of powder particle size.

As previously mentioned, the cooling rate of each powder particle effects its resulting microstructure. Finer microstructural sizes result from faster cooling particles. Since cooling rate is a direct function of powder size, the microstructural feature size (grain size, secondary dendrite arm spacing, etc.) also varies with powder particle size, though the dependence of microstructural feature size is stronger on cooling rate than powder size due to varying degrees of undercooling. Despite the variation in undercooling between particles of equal size adds a degree of variability in actual cooling rate and powder particle size, there is still a solid relationship between powder particle size and microstructural feature size. This relationship can be measured experimentally, as shown in Figure 21.

Also shown in Figure 21 is the theoretical calculation of the relationship between microstructural feature size and powder particle diameter. As mentioned, the relationship between secondary dendrite arm spacing and powder cooling rate was given in Equation 34. This equation is also applicable to microstructural feature size (in this case also referred to as grain size) when the grain size is simply substituted in place of secondary dendrite arm spacing. Combining Equation 33 with Equation 6,

$$\left|\frac{dT_d}{dt}\right| = \frac{12}{\rho C_p}\left(T_d - T_g\right)\frac{k_g}{d^2} \tag{6}$$

Relating powder particle cooling rate, $\frac{dT_d}{dt}$, and powder particle diameter, d, an equation for microstructural feature size as a function of powder particle size can be calculated,

$$\lambda = \lambda_0\left(\frac{12}{\rho C_p}\left(T_d - T_f\right)\frac{k_g}{d^2}\right)^{-n} \tag{35}$$

The results of this equation are shown compared to the experimental results in Figure 21 for Al 6061.

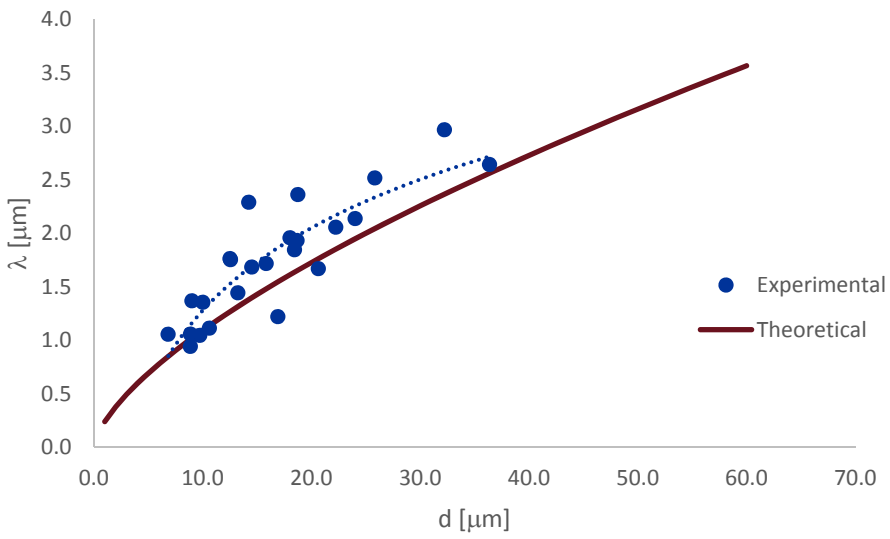

Figure 21. Experimental and theoretical comparison of the relationship between powder particle diameter, *d*, and microstructural feature size, λ.

4.6 Elemental Impact Factor

Easily, effectively, and inexpensively altering the chemical composition of alloys to determine predicted equilibrium phases by modeling played a major role in evaluating alloys to be used in the cold spray process. There are nearly infinite possible combinations of elemental composition, even just altering elements already in a given alloy. In an effort to quantify the effects that elements have on the presence of equilibrium phases, an elemental impact factor, Ψ, was created. This elemental impact factor determines the impact that a particular element has on a given equilibrium phase at a particular temperature. Figure 22 depicts the significance of the impact factor. In the schematic of the isopleth on the left, the vertical lines represent various concentrations of the varied element in the diagram. The plot on the right shows the concentration of a given equilibrium phase at the corresponding elements.

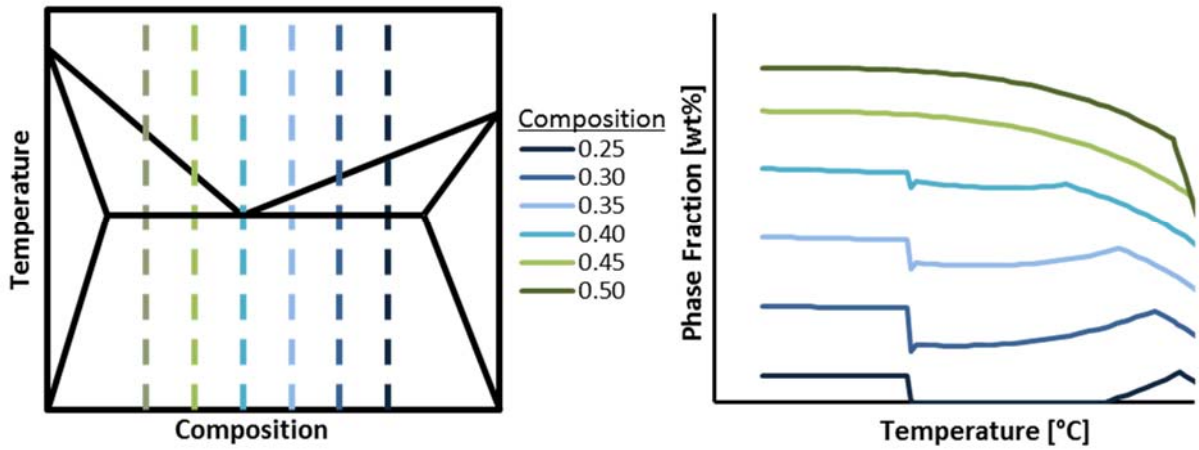

Figure 22. Schematic showing an example of the elemental impact factor for a fictional system.

An equation for this factor is given by,

$$\psi^{phase}_{element,Temp.} = \frac{\Delta wt\%\ Phase}{\Delta wt\%\ Element} \tag{36}$$

An example using Figure 23 with Equation 36 yields, for the elemental effect of Fe (left) on the alpha phase at 575°C,

$$\psi^{Phase}_{Element} = \psi^{\propto}_{Fe,575°C} = \frac{\Delta wt\%\ Phase}{\Delta wt\%\ Element} = \frac{2.07 - 0}{0.5 - 0} = 4.1$$

Calculated in the same way, the Ψ value for the effect of Cr on α, or $\Psi^{\alpha}_{Cr,575°C}$ is 1.9. Comparatively speaking, Fe has about double the effect on the alpha phase present at 575°C.

Using the same method, the elemental impact factor was created for every element and phase over a variety of compositions and temperatures. The equilibrium phase fraction raw data was calculated in JMatPro then manipulated in Microsoft Excel using a Visual Basic macro to calculate Ψ.

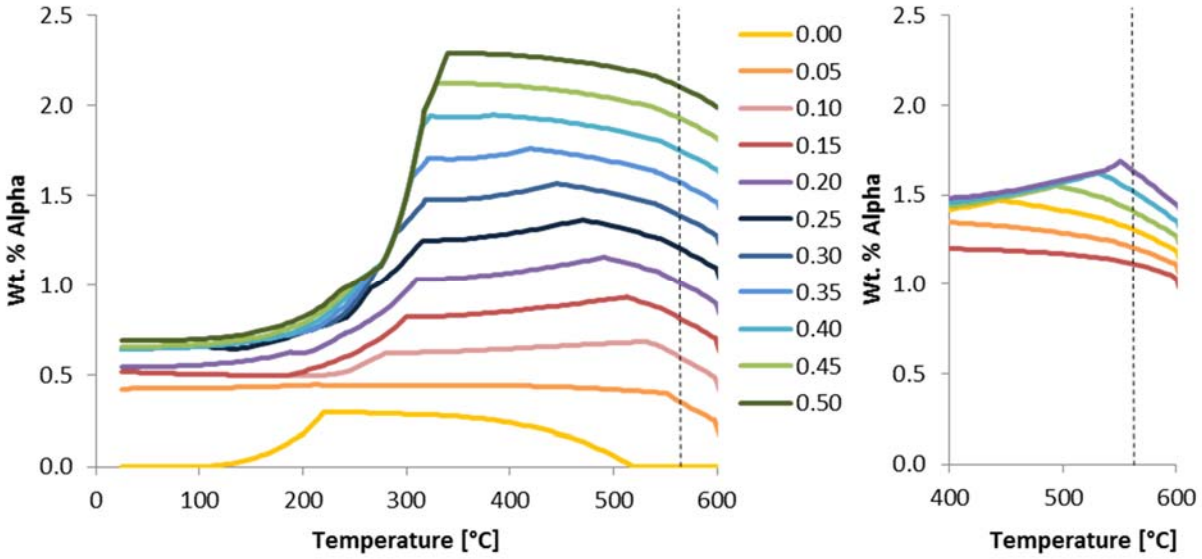

Figure 23. Variation of predicted equilibrium alpha phase in Al 6061 with a concentration variation of left) Fe, and right) Cr. The temperature of 575°C is represented by the dashed vertical lines.

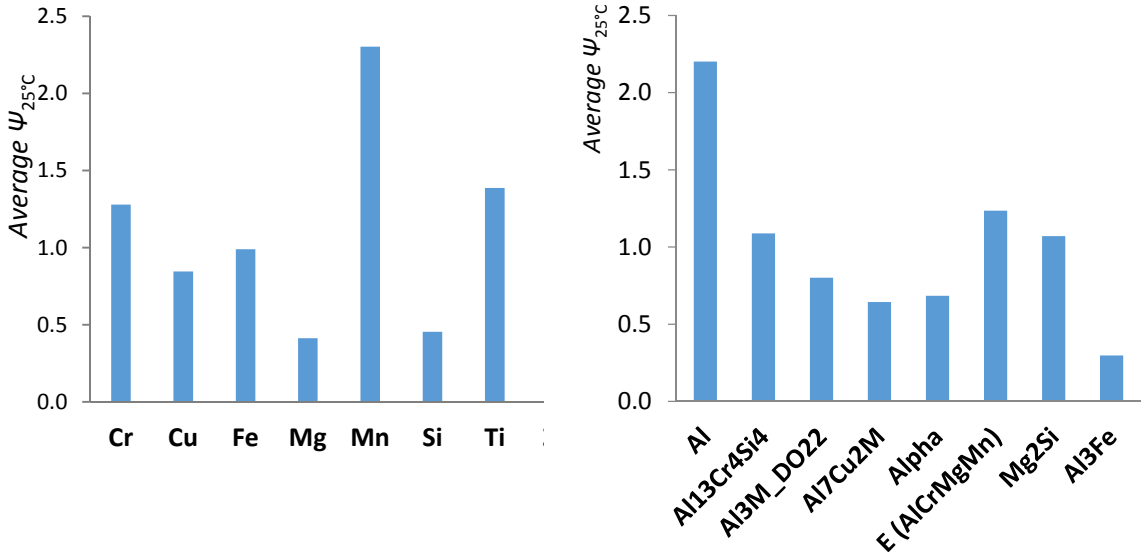

Figure 24. Average magnitude of the elemental impact factor, Ψ, for Al 6061 at 25°C for (left) each element and (right) each equilibrium phase present at this temperature.

Shown in Figure 24 (left), manganese appears to have the greatest influence on phases at room temperature. Figure 24 (right) reveals that the E (Al,Cr,Mg,Mn) phase is most easily influenced, however it only makes up 0.2 wt% of the alloy at that temperature. The Mg_2Si phase is also more easily influenced by concentration changes, while the Al_3Fe phase is less easily influenced, and therefore may require more significant concentration changes to be mitigated or created.

4.6.1 Negative Impact Factor Considerations

An update to the impact factor includes distinction between positive and negative impact factors. For instance, the addition of one element may cause an increase in quantity of one phase while reducing the amount of a different phase. Up to now, this section considered only the magnitude (taken by the absolute value) of the phase predicted.

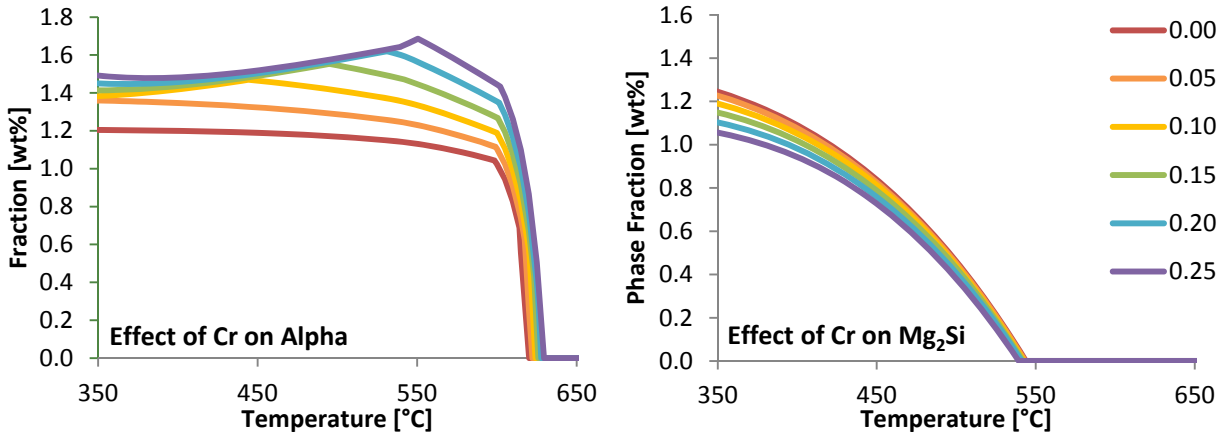

Figure 25. Equilibrium phase fractions of Alpha (left) and Mg2Si (right) as a result of varying the Cr concentration in Al 6061 between 0.0 wt% and 0.25 wt%.

An example of the differentiation between positive and negative impact factors are shown in Figure 25. As the concentration of chromium increases, the amount of the secondary phase alpha (not to be confused with the matrix phase, sometimes referred to as an alpha phase) increases at all temperature ranges. Contrasting, with this same increase in chromium concentration comes a *decrease* in the amount of Mg_2Si phase. The quantitative impact factors are given in Table 3. Note the negative effect that chromium has on the M g_2Si phase, particularly at lower temperatures.

Table 3. Elemental impact factor for the effect of chromium on the alpha and Mg_2Si phases.

T [°C]	Ψ_{Alpha}	Ψ_{Mg2Si}
350	1.1	-0.8
450	1.3	-0.4
550	2.2	0.0

Figure 26 contains the elemental impact factors for the matrix phase and most abundant secondary phases for each element in Al 6061 at 25°C. Here it is clearly depicted which elements impact, positively or negatively, the amount of equilibrium phases present. For example, the addition of any element will not decrease the amount of the Al_7Cu_2 phase.

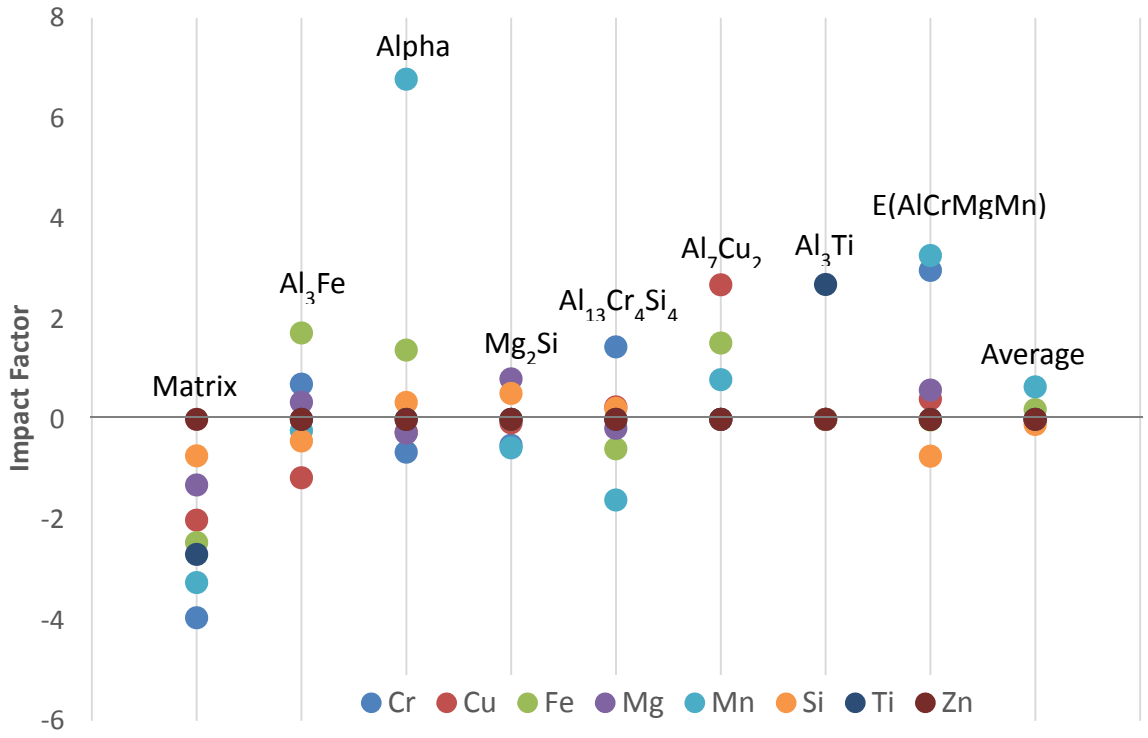

Figure 26. Compilation of the elemental impact factors for the matrix and most abundant secondary phases present in Al 6061 at 25°C.

It is evident that the addition of any of the elements, with the exception of Al, decreases the amount of the matrix phase, and therefore increases the amount of secondary phases. The impact factor can be calculated for the secondary phases as an entirety and is shown in Figure 27.

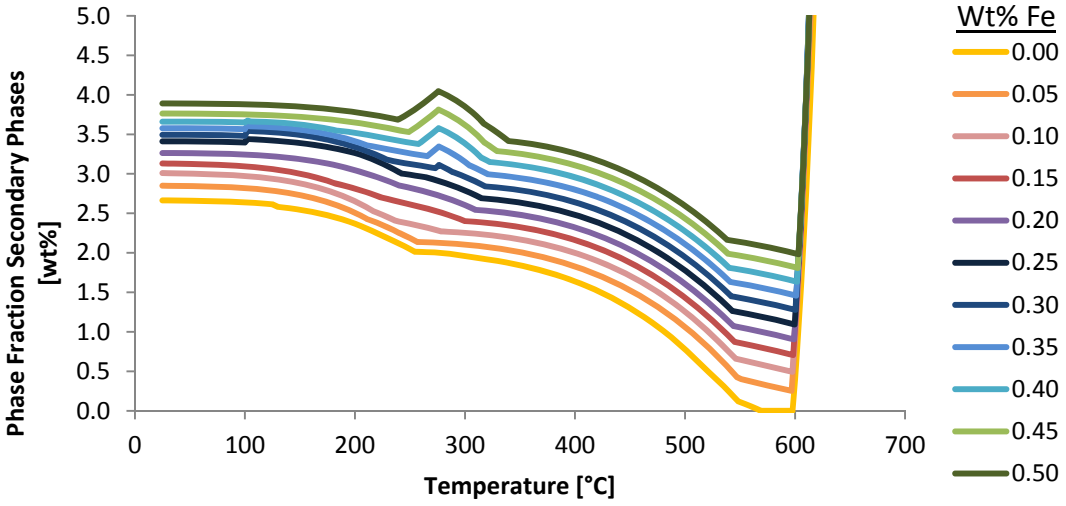

Figure 27. Elemental impact factor for the summation of the secondary phases present in Al 6061 at 25°C.

4.6.2 Metastable Impact Factors

In addition to calculating the impact factor for equilibrium phases, it can also be calculated for metastable phases. Currently, due to the limitations of the kinetic and thermodynamic software utilized, the only way to calculate phase fraction diagrams for metastable phases requires the suspension of phases suspected or known to be absent at desired conditions. An example of the phase fraction plot for a metastable phase is shown in Figure 28. The metastable phase is the β'' phase, which is a metastable precursor to the stable Mg_2Si phase. This is obviously undesirably due to the previous knowledge about the present system. This knowledge may be acquired by experimental observation or alternatively, kinetic diagrams can be calculated to determine if certain phases have enough time to form on solidification (CCT diagrams) or on aging or heating (TTT diagrams).

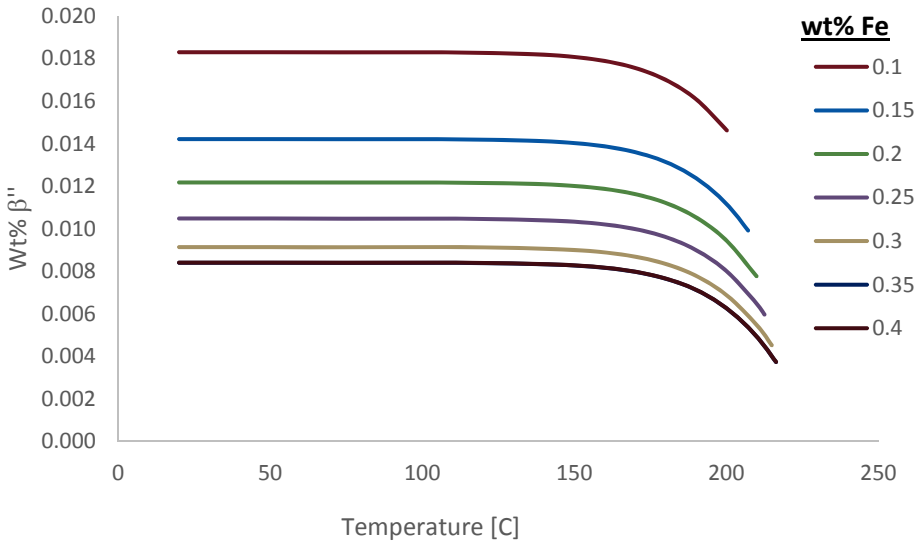

Figure 28. Phase fractions of β'' phase as a function of varying iron concentration.

4.6.3 Physical Interpretation of the Impact Factor

It is important to understand the physical meaning behind the behavior of phases shown in plots such as in Figure 25. One example of such behavior is observed in the phase fraction diagram in Figure 29**Error! Reference source not found.**. The abrupt changes in phase fraction can be correlated to phase boundaries shown in Figure 30**Error! Reference source not found.**. The phase changes corresponding to these changes are given in Table 4.

Table 4. Phase changes corresponding to the features given in the two previous plots.

Feature #	Symbol	T Range [°C]	Description
1	○	300	Maximum amount of Mg_2Si
2	△	350	Dissolution of $Al_9Fe_2Si_2$
3	◊	450-500	Formation of Mg_2Si
4	□	600	Formation of $Al_{15}Si_2M_4$

5	*	50	Transformation from Al_7Cu_2Fe to Al_2Cu

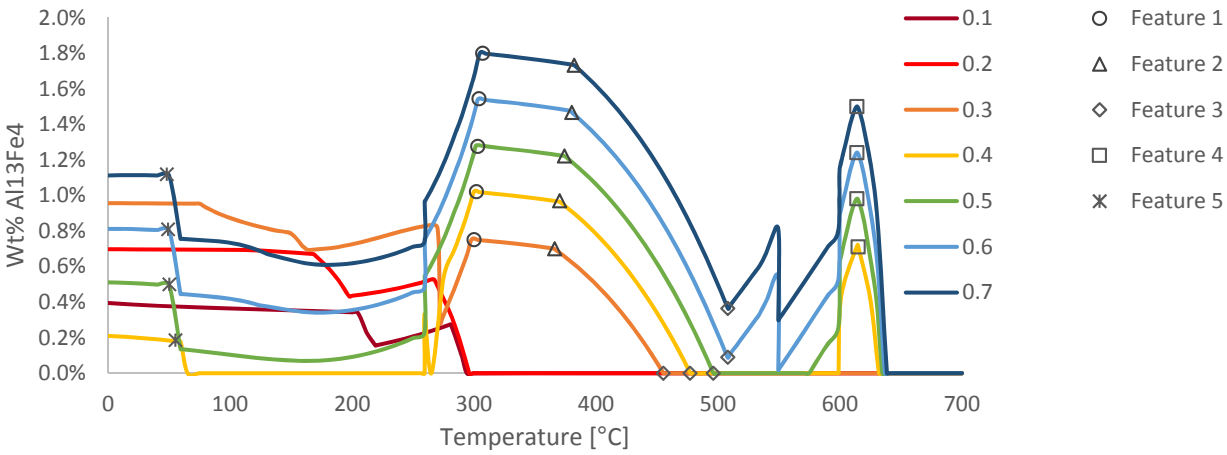

Figure 29. Effect that varying the concentration of iron on the equilibrium $Al_{13}Fe_4$ phase amount. The features are identified in the equilibrium isopleth in the following figure.

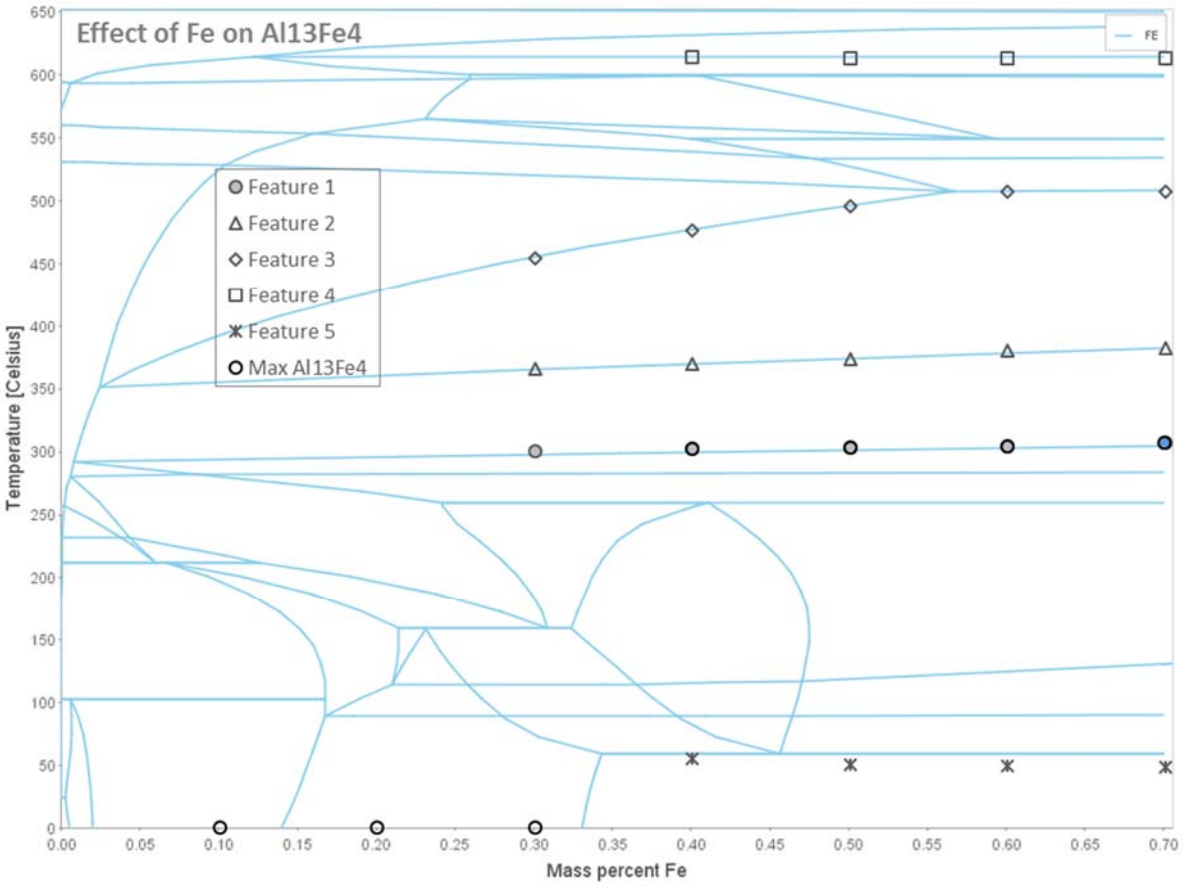

Figure 30. Equilibrium isopleth of Al 6061 with varying amounts of iron. The features (Feature 1-5) are corresponding to the behavior of equilibrium phases shown in the previous figure

4.6.4 Applications of the Elemental Impact Factor

The elemental impact factor is a quantitative way to determine the impact a given element has on any phase at a specific temperature. This is most useful when there are known beneficial or deleterious phases present in a system. Some comments about practical uses of the impact factor,

- For example, if a manufactured part is observed to fail due to crack initiations at a known phase (or multiple phases), the impact factors for elements in the alloy can be calculated for that phase. Elements with a negative impact factor, meaning the addition of that element decrease the amount of phase under investigation, could be added to the system. This is especially beneficial in cases where undesired phase are caused by the presence of impurity elements which cannot be removed from the alloy.
- Also, elements with a positive impact factor are known to increase the amount of phase under consideration. If possible, these elements could be reduced from the alloy during production.
- Similarly, for the formation of desired phases, elements with a positive impact factor could be increased to promote the amount of the desired phase and elements with a negative impact factor could potentially be decreased, though the addition of elements is typically easier than the reduction of elements, unless the alloy is made from scratch.
- Finally, the addition of elements not traditionally present in the alloys being used may be examined with the impact factor to determine potential eligible elements which may increase or decrease the amount of desired or deleterious elements.

In the case of all of the above examples, the desired and/or undesired phases must first be known in order to find the impact factor useful. This often requires experimental investigation into the material and its failure mechanisms.

However, once these phases are known, the benefits may be great. As with many computation models, the time, resources, and monetary savings from modeling as opposed to experimentation are significant. Of course, models cannot be substituted entirely for experiments, the impact factor model can be used to determine calculated candidate chemical compositions for alloys.

4.6.5 Impact Factor Limitations

Obviously this elemental impact factor approach has limitations and exceptions. First of all, phase stoichiometry is not accounted for, so resulting phase predictions may show discontinuous behavior at specific concentrations due to this stoichiometric effect. Also, at certain concentrations, phase fractions actually cross one another, resulting in an inaccurate impact factor at those concentrations.

Once phases are identified as being beneficial or detrimental to the cold spray process, these predictive models will shows alterations in which they can be created or avoided, respectively. In addition to the properties discussed in this section, work is being done to complete this predictive model stage to include grain and secondary phase size results. Significant data analysis has been performed on this impact factor and will be presented in future work.

5 MECHANICAL PROPERTY MODELS

Two models were used to determine the mechanical properties of the powder particles, both as a function of powder particle size. The first model is based on the results of the JMatPro mechanical properties model and will be referred to as the JMX model. The second is an in-house model containing the summation of several strengthening terms. This will be referred to as the Additive Model. The JMX model calculates both yield strength and hardness, while the Additive Model calculates only yield stress, which can be converted to hardness. Experimental microhardness measurements on powder particles as a function of their diameter were made to experimentally validate the model.

5.1 JMX MECHANICAL PROPERTIES MODEL

The JMatPro software package calculates yield stress, ultimate tensile stress, and hardness values as a function of material cooling rate, as discussed in 3.5.2.1.

First, JMatPro is used to calculate the mechanical properties as a function of cooling rate for the exact alloy composition desired. The range of cooling rates calculated by the software is limited, between 0°C/s to 100°C/s. It was shown in the solidification modeling, Section 4.5, that cooling rates for Al-based powder particles formed during atomization were significantly higher, up to 10^7°C/s for the smallest particles. Curve fitting techniques, then extrapolation to higher cooling rates were performed.

Next, the cooling rates were converted to grain size using the relationship in Equation 33 producing the mechanical properties as a function of grain size. Grain size was then converted to powder particle size using both the experimental relationship between grain size and particle size, as well as the theoretical relationship given in Equation 34. The resulting relationships are given in Figure 31 and Figure 32.

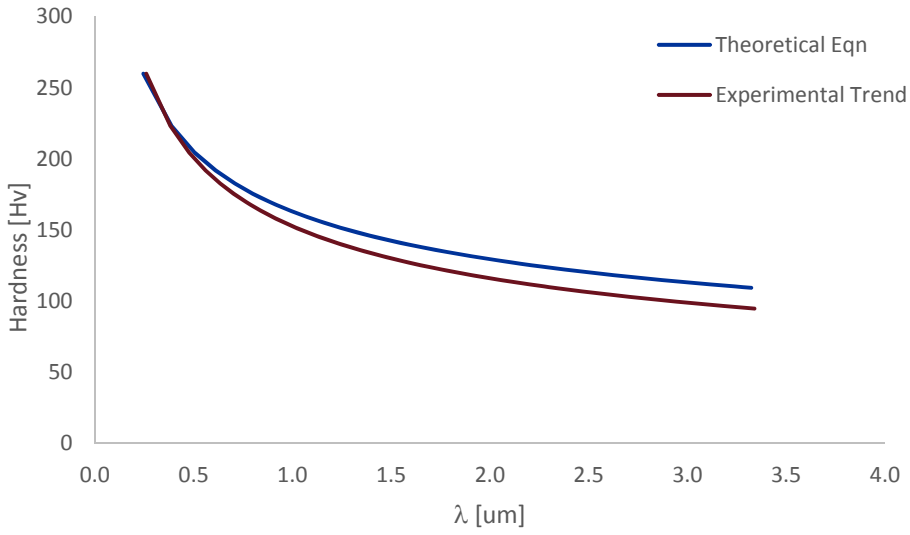

Figure 31. Hardness values calculated using the JMX model converted to hardness as a function of microstructural feature using both the theoretical relationship and experimental trend between cooling rate and microstructural feature size.

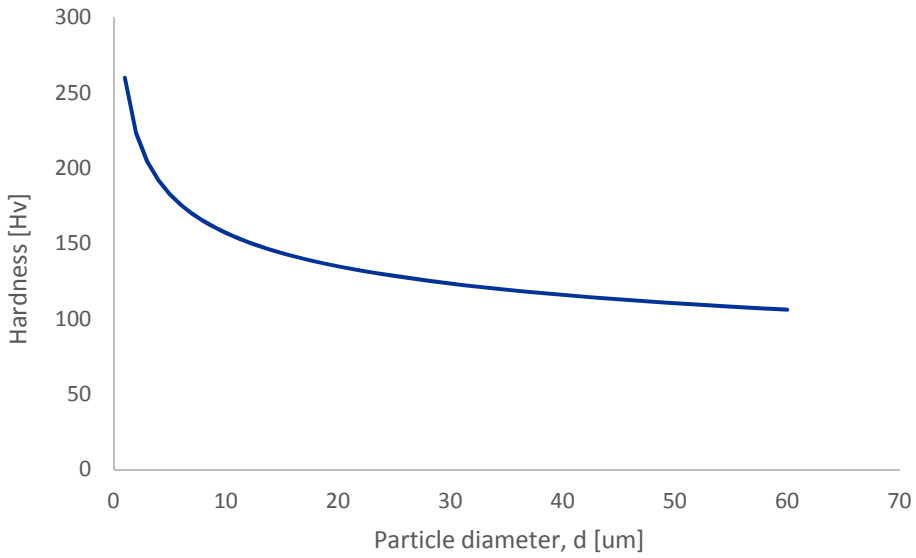

Figure 32. Hardness as a function of powder particle diameter. Powder particle diameter in this plot was calculated using the theoretical relationship between particle cooling rate and diameter.

5.2 Additive Mechanical Properties Model

The additive mechanical properties model approximates yield stress as a function of powder particle diameter and is the resulting summation of several strengthening terms given by the equation,

$$\sigma_{YS(d)} = \sigma_o + \Delta\sigma_{ss} + \Delta\sigma_{mic}(d) + \Delta\sigma_{ppt}(d) \tag{37}$$

Where $\sigma_{ys}(d)$ is the yield stress of a powder particle of diameter, d; σ_o is the intrinsic yield stress of the matrix phase, σ_{ss} is the strengthening due to solid solution, $\sigma_{mic}(d)$ is the strengthening due to microstructural features (i.e. grain size) of the matrix phase, and $\sigma_{ppt}(d)$ is the strengthening contribution from precipitates.

A brief overview of each strengthening term is given below, but a more comprehensive description will be given in other publications.

5.2.1 Solid Solution Strengthening (SSS)

Strengthening due to solid solutioning is given by the equation,

$$\Delta\sigma_{ss} = \sum_i x_i \Omega_i \tag{38}$$

Where x_i is the atomic concentration of each element in the alloy and Ω_i is the strength contribution to the FCC Al matrix per atomic amount of each element added, as given in the ASM Handbook.

5.2.1.1 Dependencies of the SSS Term

This term is dependent only on the composition of the alloy.

5.2.1.2 Heat Treatment Effects from the SSS Term

This term is directly unaffected by effects from heat treatment of the powder material. Potentially, there may be indirect effects due to the formation of additional secondary phases and precipitates diluting the concentration of alloying elements in the matrix.

5.2.2 Microstructural Strengthening

Strengthening due to the microstructure of the matrix phase is approximated by Hall-Petch behavior,

$$\Delta\sigma_{mic}(d) = k_{gs}\lambda^{-0.5} \tag{39}$$

Where k_{gs} is the Hall-Petch constant and λ is the microstructural feature size, both of the matrix phase. It is evident from this relationship that hardness of each powder particle is inversely proportional to the feature size, which in turn is directly proportional to the powder particle size, as shown experimentally and theoretically in Figure 21, resulting in increasing hardness with decreasing powder particle size. This term is obviously only valid in regions where microstructural features are present. For instance, the yield stress of the extremely small particle size with seemingly no microstructure present will not be considered by this equation.

5.2.2.1 Dependencies of the Microstructural Strengthening Term

This term is dependent on the chemical concentration of the alloy. Also, there is a very strong dependence of this term on the powder particle size due to the direct relationship between the powder particle size and its microstructural features, as discussed in Section 4.5.1. Either the theoretical or experimental relationship between powder size and microstructural feature size may be used.

5.2.2.2 Heat Treatment Effects of the Microstructural Strengthening Term

The effect of heat treatment was studied for two heat treatment conditions in an experimental nature only. Grain size as a function of powder particle size was measured for as-received powder and powder heat treated for 24 hours at 200°C and 230°C. There was a 5-10% grain size increase between the as-received at 200°C treated and between the 200°C and 230°C treated.

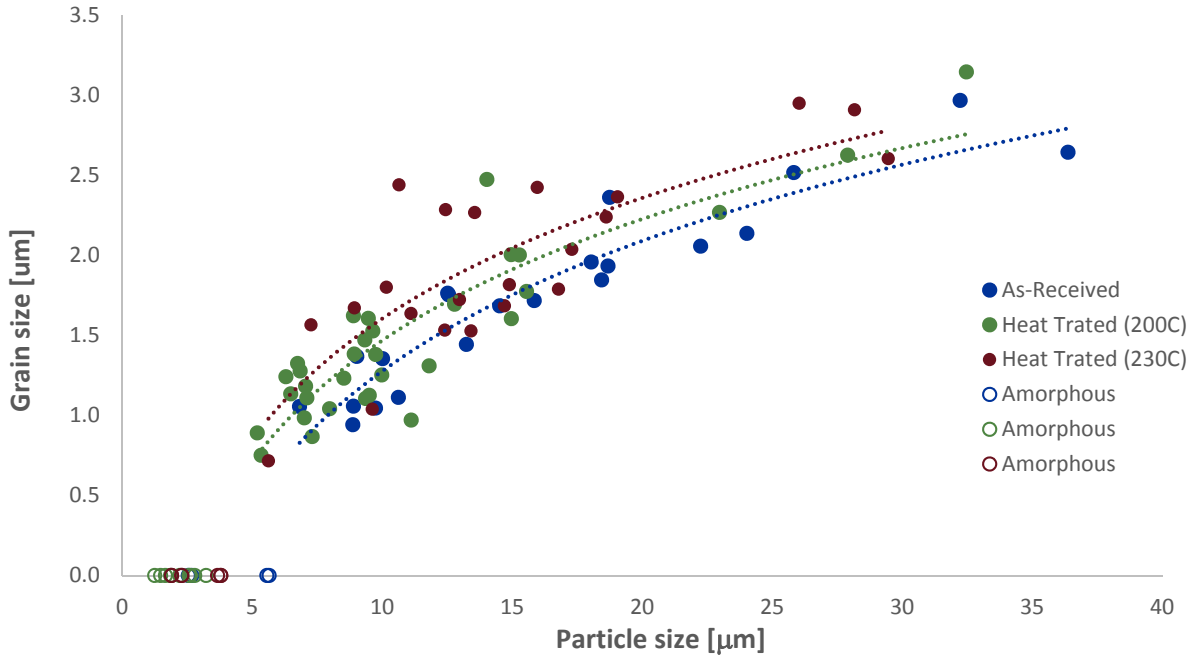

Figure 33. Grain size as a function of powder particle size for as-received powder and powder heat treated for 24 hours at 200°C and 230°C.

This increase in grain size with powder particle size results in a decrease in hardness of powder particles having undergone heat treatment.

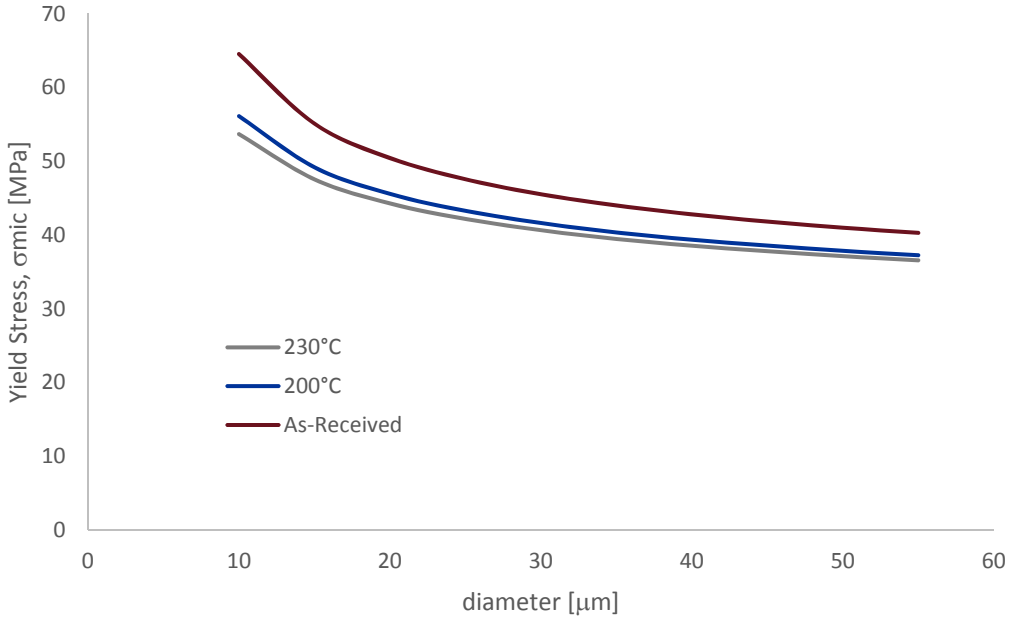

Figure 34. Yield stress contribution (σ_{mic}) due to grain size *only* as a function of powder particle diameter, in accordance with Equation 38.

In order to allow for the automation of this hardness model, theoretical approximation of grain size growth as a function of heat treatment recipe should be determined. One such approach may be the grain growth or Ostwald Ripening relationships.

5.2.3 Precipitation Strengthening

The strengthening term due to precipitates currently considers incoherent, unshearable particles. It is modeled using the Ashby-Orowan relationship,

$$\Delta\sigma_{ppt,i} = \sum_i 0.84M \left[\frac{1.2Gb}{2\pi L_i}\right] ln\left(\frac{r_i}{b}\right) \tag{40}$$

where M is the Taylor factor, r_i is the particle radius of phase i, b is the burger's vector, G is the shear modulus, r is the particle radius, and L_i is the inter-particle spacing of phase i, given by,

$$L_i = \left(1.23\sqrt{\frac{2\pi}{3f_{ppt,i}}} - 2\sqrt{\frac{2}{3}}\right) r_i \tag{41}$$

where f_{ppt},i is the fraction of phase i. This amount can be approximated by utilizing the thermodynamic and kinetic diagrams created in previous sections. An equation to quantify this value is given by,

$$f_{ppt,i} = f_{ppt,i,C} + x_{ppt,i} f_{ppt,i,max} \tag{42}$$

$f_{ppt,i,C}$ is the amount of phase i that was formed on cooling, though since gas atomization has extremely high cooling rates, this value is nearly always zero. It can be calculated using a CCT diagram for precipitate i. An example is shown in Figure 35 I.

$f_{ppt,i,max}$ is the maximum amount of phase i that may be formed according to thermodynamic equilibrium calculations, shown graphically in Figure 35 II. When this term is multiplied by $x_{ppt,i,T}$, which is the percentage of the maximum amount of phase i that actually forms, an actual amount of formed phase i is determined. $x_{ppt,i,T}$ is calculated by utilizing the Avrami behavior of percent phase transformed by transforming the TTT diagram in Figure 35 III to a more model-friendly format, determining the phase fraction transformed as a function of time and temperature, shown in Figure 36.

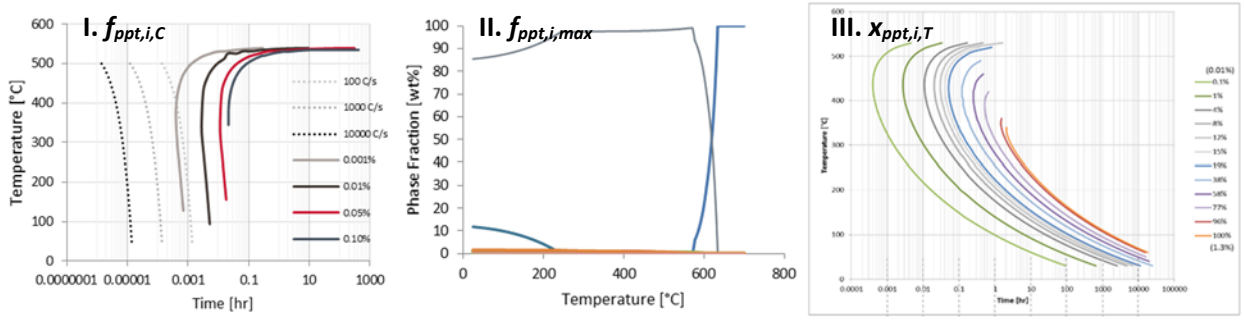

Figure 35. Plots used in the calculation of the fraction of a given phase used in the precipitation equations. I) The fraction of phase i formed during cooling. II) The maximum amount of phase i that could be formed. III) The percentage of the maximum phase i that is actually formed during either natural aging or a heat treatment.

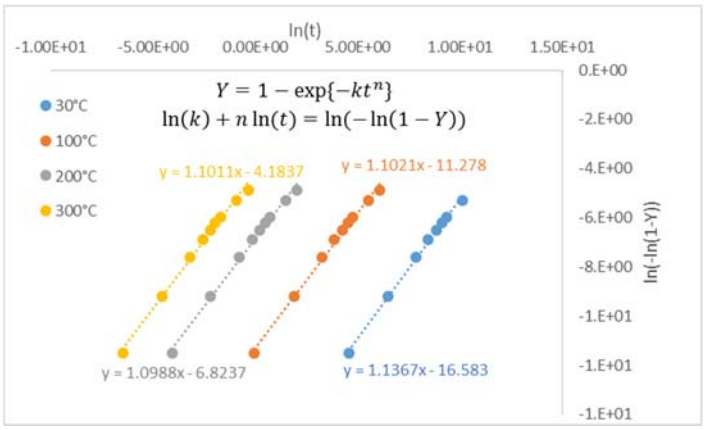

Figure 36. Phase fraction (of maximum amount possibly formed) as a function of time for various temperatures. This data is used in the quantification of amount of secondary phases formed.

5.2.3.1 Dependence of the Precipitation Strengthening Term

The precipitation strengthening term is dependent on alloy composition, and aging/heat treatment time and temperature. Higher temperatures and longer times produce a higher fraction of particles, though since particle also grow during these events, their contribution to strength will eventually decrease. TC-PRISMA software will be utilized to predict precipitate size to be of consideration in this term.

5.2.3.2 Heat Treatment Effects of the Precipitation Strengthening Term

As mentioned in the previous section, increasing time and temperature exposure of the powders will increase the phase fraction of secondary phases, but also increases the average size of the secondary phase particles, thus eventually decreasing the strengthening effect of the precipitate. TC-PRISMA software will be utilized to determine particle sizes as a function of time and temperature and will thus be factored into this strengthening term.

5.2.4 Model Results

The results of the additive mechanical properties model are given in Figure 37. At small particle diameters, the microstructure has a higher influence on yield stress than it does at larger particles, due to the Hall-Petch behavior of increasing strength with decreasing grain size. Also, the solid solution strengthening term and matrix term remain constant since this current model does not consider precipitation growth that depletes the matrix phase of any dissolved elements. Finally, the precipitation strengthening term also decreases with increasing particle size because the cursory assumption of the model is to relate precipitate size with particle size based on experimental observation. This method will be changed in future versions to utilize kinetic TC-PRISMA software to predict particle sizes.

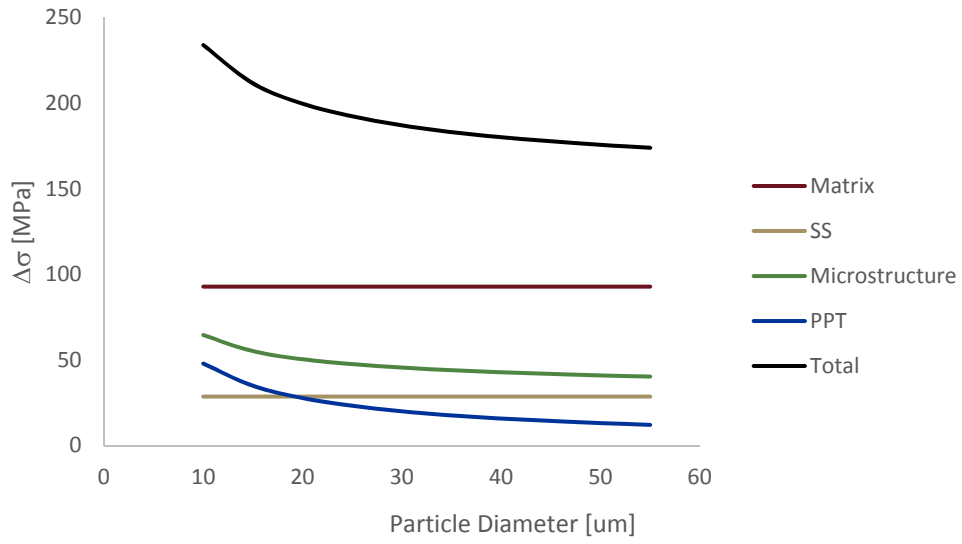

Figure 37. Result in total yield stress as a function of powder particle diameter. Also shown are the individual contributions by the solid solution strengthening (SS), microstructure, and precipitates (PPT).

5.3 Comparison of Models & Experiments

5.3.1 Model Comparison & Discussion

A comparison of the resulting yield stress as a function of powder particle diameter for both the JMX model and the additive model (DB Model) is given in Figure 38.

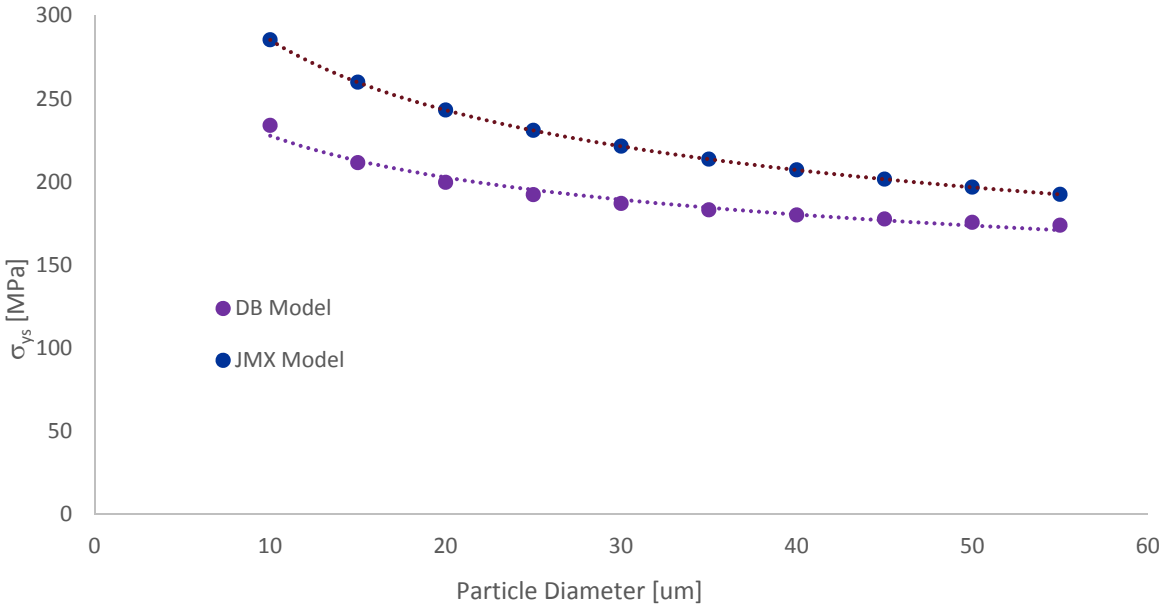

Figure 38. Yield stress comparison of both the Additive and JMX models as a function of powder particle diameter.

5.3.2 Experimental Procedure & Results

Due to the extremely small size of the powder particles used in the cold spray process, it was difficult to obtain mechanical properties of the individual, unconsolidated particles. A method for measuring hardness of individual particles was developed and used to approximate yield stress of the particles.

Powder particles were mounted in a clear epoxy resin, polished, then analyzed in the nanohardness indenter where one nanohardness measurement was taken at the center of the exposed surface area for each particle. Careful documentation was recorded to map the location of each powder particle on the sample with the correct nanohardness reading. To determine the particle diameter, the sample was then etched and grain size was measured for each particle in which a nanohardness measurement was taken. The top 5% of the largest grain sizes measured were assumed to be sliced at the midpoint of the grain and this number was then used as the grain size for the respective particle.

A more accurate way to do this measurement will be to first sieve the powders into small size ranges, then measure the nanohardness of each range.

The experimental and theoretical relationships between grain size and powder particle size were then used to convert grain size to particle size, resulting in nanohardness as a function of powder particle size. Nanohardness was subsequently converted to hardness and then yield stress. Results are given in Figure 39.

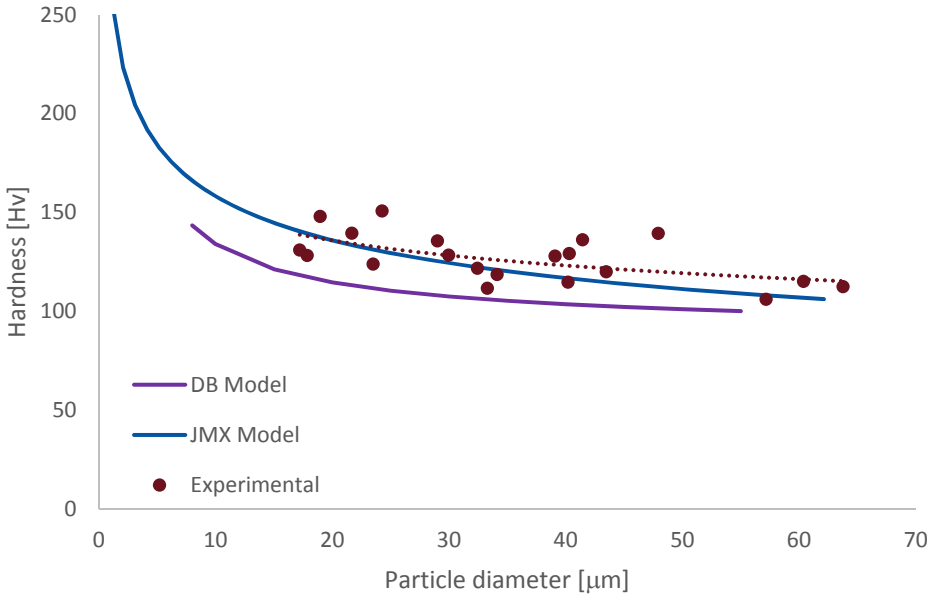

Figure 39. Hardness as a function of powder particle diameter for the additive hardness model and JMX hardness model compared to experimentally measured data.

Experimental hardness measurements were very similar to theoretically predicted values. There was a 0-8% difference between experimental and JMX model results and a 9-14% difference between experimental and the additive model.

The experimental technique of nanohardness determination was obviously a cursory approach and may be certainly contribute to some of the difference in values. Also, the consideration of only semicoherent and coherent particles in the precipitation strengthening contribution term, and the current consideration of only one precipitate for the alloy discussed, may explain the lower than expected predicted values of the additive model results.

6 ADDITIONAL EXPERIMENTAL CONTRIBUTIONS

6.1 EXPERIMENTAL OVERVIEW

Limited model verification has been performed. Verification of commercially available alloys was performed due to their ease of availability. Due to equipment and time constraints, customized alloys were not made and therefore not analyzed.

The alloys that were available were analyzed using x-ray diffraction (XRD), scanning electron microscopy (SEM), transmission electron microscopy (TEM), energy dispersive spectroscopy (EDS), micro and nanohardness, and optical microscopy.

Due to the minute size and low phase fraction of the secondary phases formed in Al 6061, SEM/EDS and XRD were used with limited success to identify and quantify the secondary phases. TEM yielded the best results, though access to the TEM was limited. As an aside, future work using alloys with predicted higher secondary phase concentration will be explored.

6.1.1 Materials

Several aluminum alloys from the 5xxx and 6xxx series have been studied. Chemistries for alloys used are given in Table 1. Three powders used in this characterization were Al 5083 powder (Valimet), Al 6061 powder (Valimet), and nanocrystalline Al 5083 powder (N-werks). This paper contains several characterization methods employed to develop a comprehensive fundamental understanding of powder and cold sprayed Al 6061 as well as verify certain model predictions. Both powders and consolidated cold spray material were characterized to develop a relationship and correlation between their respective properties.

6.1.2 Material Preparation

For microscopy, the Al 6061 powder was cold mounted in resin while hot compression mounting was used for the consolidated material. Both samples were ground to 1200 grit SiC paper, polished with 1.0, 0.3, and 0.05 µm water-based alumina suspensions, and polished with MasterMet® colloidal silica on a MicroCloth®. The samples were etched with a 0.5% HF etchant for 90 seconds. For TEM, the samples were prepared using a focused ion beam (FIB).

6.2 BASIC MATERIALS CHARACTERIZATION

6.2.1 Particle/Grain Size and Morphology

Materials produced by cold spray are non-isotropic, thus the microstructure varies significantly based on the direction of the cold spray stream, seen in Figure 3B. SEM depicting this non-isotropic behavior are given in Figure 40. Figure 40a shows a cross section of etched Al-6061 powder, Figure 40b shows a cross

section of the XY face of cold spray consolidated Al 6061, sprayed from the powder in Figure 40a. Figure 40c is the same cold spray consolidated material shown in Figure 40b, but cut so that the YZ face is captured. Particle and grain boundaries are seen.

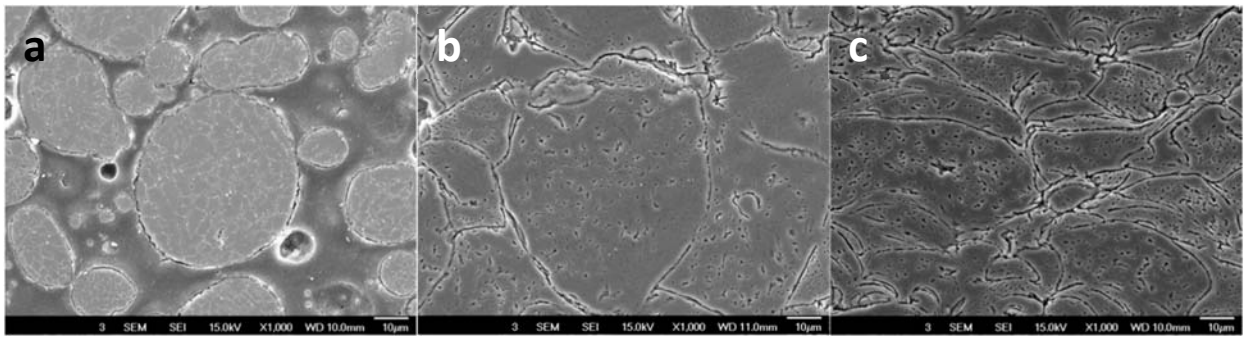

Figure 40. SEM images of cross sections of a) Al 6061 powder, b) XY face, and c) YZ face etched with 0.5% HF solution for 90 seconds. Scale bars read 10 μm. Face directions are shows in Figure 1 (right).

The aspect ratios of powder particles and grains were determined by dividing the respective particle or grain major axis by the minor axis. This allowed for a relative comparison of the grain size and morphology from the powder to the two directions of the cold sprayed material. These average aspect ratios are shown in Table 5.

Table 5. Average aspect ratios of particles and grains in Al 6061 powder and consolidated cold sprayed material.

	Particle Aspect Ratio	Grain Aspect Ratio
Powder	1.09	1.41
Cold Sprayed XY Face	1.44	1.40
Cold Sprayed YZ Face	2.22	2.77

The aspect ratio of the grains and particles is unchanged from the powder to the XY face, but doubles in the YZ face. This is a result of the plastic deformation occurring during the cold spray process. On impact, the particles impinge on previously sprayed particle layers, causing the particles to appear flattened and the grains to become elongated in the YZ face. This is important because an ideal powder particle material for the cold spray process would need to be able to be beneficially plastically deformed to this degree.

6.2.2 X-Ray Diffraction

X-ray diffraction was performed on Al 6061 powder and cold sprayed Al 6061 in order to determine if new phases formed during the cold spray process. The XRD patterns of the Al 6061 powder and consolidated material are shown in Figure 41. There is no discernible difference between the peak locations, proving that no new phases are formed during the cold spray process. However, it is not possible to identify secondary phases with this method because they are smaller than 250 nm precipitates, and are present in less than 3% of the alloy. A slower, more comprehensive XRD scan on smaller 2θ ranges will be performed. These secondary phases can be identified using SEM and TEM with EDS. The causes of XRD peak broadening and shifting will be presented in the future.

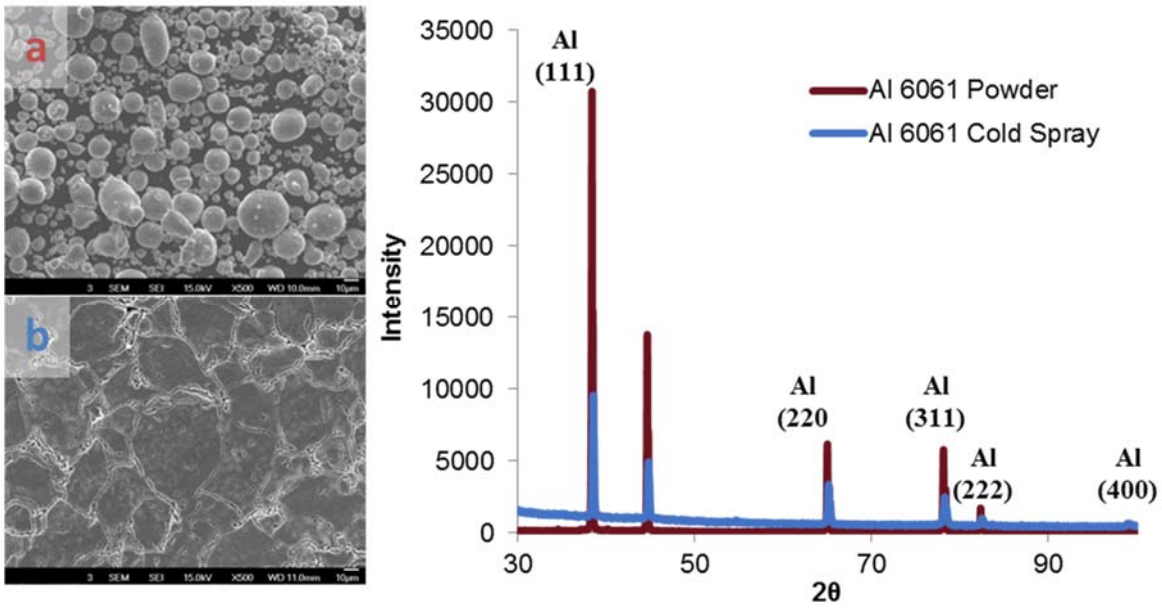

Figure 41. SEM image of a) Al 6061 powder, b) Al 6061 consolidated material, and right) XRD using Kα1 radiation.

6.3 Model Verification

6.3.1 Transmission Electron Microscopy/Energy Dispersive Spectroscopy

SEM and TEM with EDS have proved to be beneficial tools in confirming compositions of precipitates at the grain boundaries to help identify phases present. SEM work was done at WPI by Ph.D. student Baillie McNally and TEM work was done at the Advanced Materials Processing and Analysis Center at the University of Central Florida by Le Zhou.

As shown in Figure 10 in Section 4.3, the major secondary phases that are predicted by thermodynamic models are the iron-containing phases α ($Al_{47}(Fe,Mn,Cr)_{11}Si_5$) and Al_7Cu_2Fe, as well as Mg_2Si. The STEM image in Figure 42**Error! Reference source not found.** shows two types of precipitates. EDS spectra of those precipitates reveal the white phase to be one of the iron-containing phases, while the dark phase is Mg_2Si.

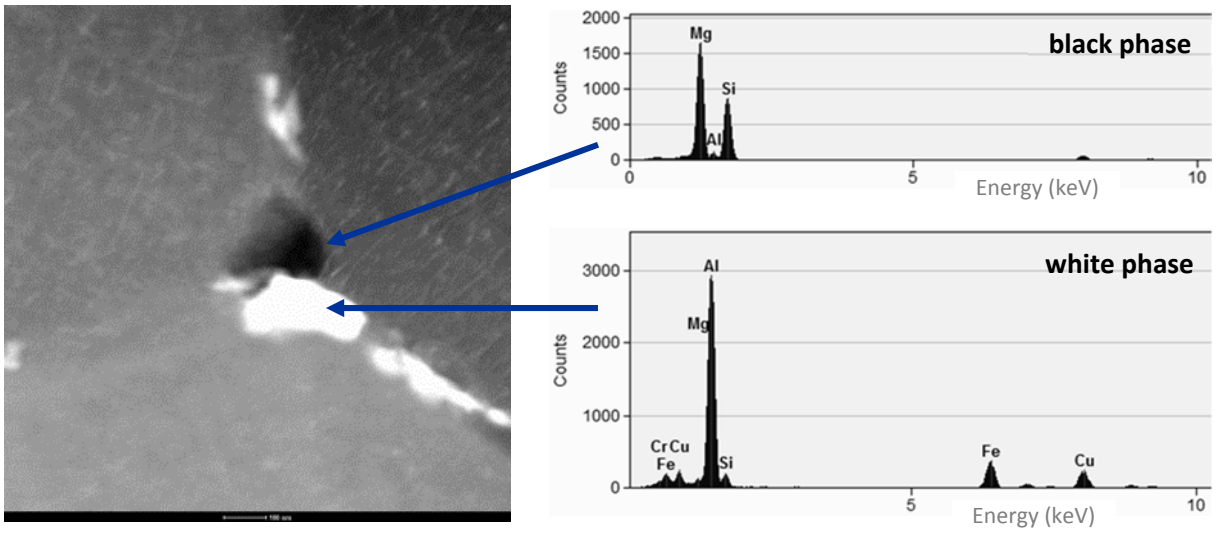

Figure 42. A) STEM image of Al 6061 powder grain boundary with corresponding EDS plots of the black and white phases detected in the image. STEM image scale bar reads 100 nm.

Corresponding TEM and EDS of Al 6061 consolidated material showed both the dark magnesium rich precipitate and the white iron containing precipitate, confirming that both types of precipitates were formed during powder production and not the cold spray process. Next, TEM diffraction patterns will be used to determine the d-spacings and ultimately confirm the phase identifications.

6.3.2 Secondary Dendrite Arm Spacing

As previously discussed in Section 4.5, there is a direct relationship between secondary dendrite arm spacing and cooling rate, given by Equation 33. The constants, λ_0 and n, in that equation were determined by fitting a power law plot to the data for Al 6061 generated in JMatPro. Rearranging Equation 33 to solve for the cooling rate yields,

$$\left(\frac{dT_d}{dt}\right) = 10^{\left\{\frac{\log(\lambda_0/\lambda_2)}{n}\right\}} \tag{43}$$

where the only unknown is the secondary dendritic arm spacing. This value can be measured from SEM images of the powder, as shown in Figure 43. The cooling rate estimated by these calculations for this powder particle is 9.6×10^4 °C/s. This cooling rate can then be used to estimate the size of the particle using the relationship in the simplified solidification model, Equation 6. Rearrangement of this equation to solve for particle size leads to,

$$d = \sqrt{\frac{12k_g(T_d - T_f)}{\frac{dT_d}{dt}\rho C_p}} \tag{44}$$

Solving this equations for this powder atomization, the diameter predicted from the simplified solidification model is 30.6 μm. The measured diameter of the powder is 37.0 μm.

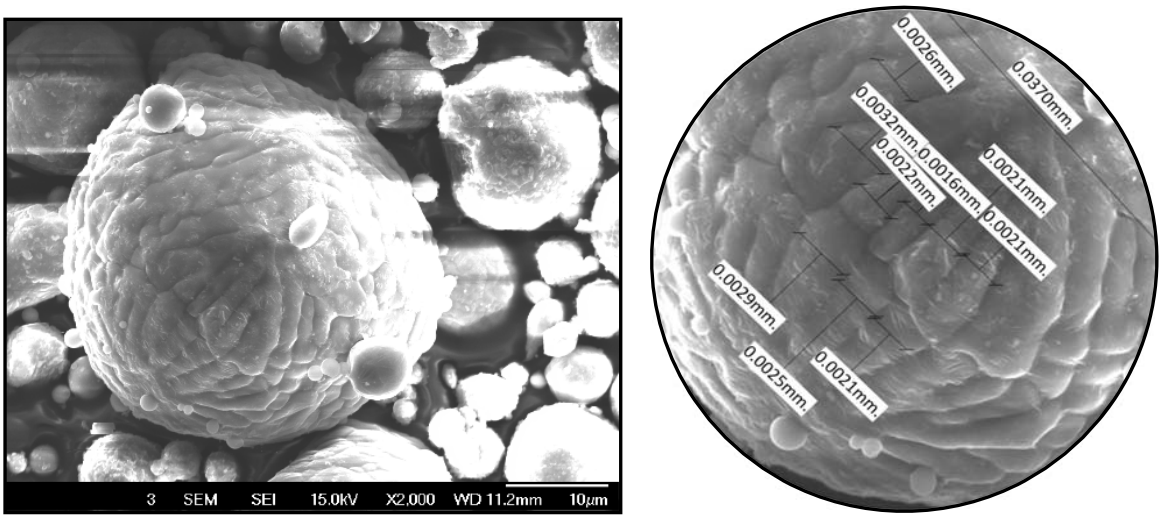

Figure 43. SEM image of a large Al 6061 powder particle. Secondary dendritic arm spacing measurements are shown in figure on the right.

7 FUTURE WORK

7.1 MODEL VERIFICATIONS

7.1.1 Nanohardness Measurements

Ideally, powder will be sorted into small size-range "bins" where nanohardness measurements can be taken on samples from each bin, ensuring measurements taken are from a specific size particle.

7.1.2 Additional Alloys Model Verification

While some of the models discussed were run using various alloys, most were only run for Al 6061. Future work will perform the model analysis for at least Al 5083, clean Al 5083, and Al 5056, as those alloys are of the most interest to the Army Research Laboratory.

Also, Al 5083 and Al 6061 both exhibit significantly larger fractions of secondary phases compared to Al 6061, hopefully making the experimental analysis to identify and quantify these phases easier.

7.1.3 Heat Treatments to Verify TTT Diagrams

Applying various heat treatments to to-be-sprayed Al powders then experimentally performing secondary phase identification and quantification will be performed to determine the accuracy of the time-temperature-transformation diagrams created using the kinetic-based models, discussed in 4.4 and shown in Figure 13, where Mg_2Si is the secondary phase of interest.

7.2 MODEL UPDATES

7.2.1 Additive Hardness Model: Precipitation Strengthening Term

Kinetic software TC-PRISMA will be utilized to predict the amount and size of secondary precipitates formed during solidification and aging/heat treatment. This will replace the current method of approximating precipitate size using experimental observations.

8 REFERENCES

1. Belsito, D.C., V.; Sisson, Jr., R.D., *Cold Spray Manufacturing for Repair*, in *Department of Defense Rapid Innovation Fund*. 2012, Department of Defense.
2. *Through-process simulation of texture and properties during the thermomechanical processing of aluminium sheets.* Acta Materialia, 2007. **55**: p. 5449-5463.
3. Allison, J., P. Collins, and G. Spanos, *From Processing to Properties: Through‐Process Modeling of Aluminum Sheet Fabrication*, in *Proceedings of the 1st World Congress on Integrated Computational Materials Engineering (ICME)*. John Wiley & Sons, Inc: Hoboken, NJ, USA. p. 9-17.
4. Crumbach, M., et al., *Through-process texture modelling of aluminium alloys.* Modelling and Simulation in Materials Science and Engineering, 2004. **12**(1): p. S1-S18.
5. Dørum, C., H.I. Laukli, and O.S. Hopperstad, *Through-process numerical simulations of the structural behaviour of Al–Si die-castings.* Computational Materials Science, 2009. **46**(1): p. 100-111.
6. Champagne, V.K., *The Cold Spray Materials Deposition Process: Fundamentals and Applications*. 2007: Woodhead Publishing Limited.
7. Champagne, V.K., et al., *The effect of cold spray impact velocity on deposit hardness.* Modelling and Simulation in Materials Science and Engineering, 2010. **18**(6): p. 065011-065011.
8. Army, U.S., *Military Specification MIL-DTL-46027K(MR)*, U.S. Army, Editor. 1998.
9. Army, U.S., *Military Specification MIL-DTL-32262 (MR)*, Army, Editor. 2007.
10. Council, N.S.T., *Materials Genome Initiative for Global Competitiveness*. 2011.
11. Kuehmann, C.J. and G.B. Olson, *Computational materials design and engineering.* Materials Science and Technology, 2009. **25**(4): p. 472-478.
12. Olson, G.B., *Materials by Design*. 2005, Springer Netherlands: Dordrecht. p. 2667-2669.
13. Olson, G.B., et al., *Precipitation Model Validation in 3rd Generation Aeroturbine Disc Alloys*. 2008.
14. Kroupa, A., *Modelling of phase diagrams and thermodynamic properties using Calphad method - Development of thermodynamic databases.* COMPUTATIONAL MATERIALS SCIENCE, 2013. **66**: p. 3-13.
15. Lukas, H.L., et al., *Computational thermodynamics: the CALPHAD method*. 2007, New York: Cambridge University Press.
16. Guo, Z., et al., *Material properties for process simulation.* Materials Science & Engineering A, 2009. **499**(1): p. 7-13.
17. Saunders, N., et al., *Using JMatPro to model materials properties and behavior*. JOM, 2003. **55**(12): p. 60-65.
18. Chakrabarti, D.J. and D.E. Laughlin, *Phase relations and precipitation in Al–Mg–Si alloys with Cu additions.* Progress in Materials Science, 2004. **49**(3): p. 389-410.
19. Yu, J.-J., X.-M. Li, and X.-Q. Yu, *Thermodynamic Analyse on Equilibrium Precipitation Phases and Composition Design of Al-Zn-Mg-Cu Alloys.* Journal of Shanghai Jiaotong University, 2012. **17**(3): p. 286-290.
20. Saunders, N. *The Modelling of Stable and Metastable Phase Formation in Multi-Component Al-Alloys*.
21. He, S.W., Y. Liu, and S. Guo, *Cooling Rate Calculation of Non-Equilibrium Aluminum Alloy Powders Prepared by Gas Atomization.* RARE METAL MATERIALS AND ENGINEERING, 2009. **38**: p. 353-356.
22. Mullis, A.M., et al., *Estimation of Cooling Rates During Close-Coupled Gas Atomization Using Secondary Dendrite Arm Spacing Measurement.* Metallurgical and Materials Transactions B, 2013. **44**(4): p. 992-999.

23. Bhuiyan, M.H., et al., *Microstructural behavior of the heat treated n-type 95% Bi2Te3-5% Bi2Se3 gas atomized thermoelectric powders.* JOURNAL OF ALLOYS AND COMPOUNDS, 2011. **509**(5): p. 1722-1728.
24. Su, Y.H. and C.Y.A. Tsao, *Modeling of solidification of molten metal droplet during atomization.* Metallurgical and Materials Transactions B, 1997. **28**(6): p. 1249-1255.
25. Hirth, J.P., *Nucleation, undercooling and homogeneous structures in rapidly solidified powders.* Metallurgical Transactions A, 1978. **9**(3): p. 401-404.
26. Zeoli, N., S. Gu, and S. Kamnis, *Numerical modelling of metal droplet cooling and solidification.* International Journal of Heat and Mass Transfer, 2008. **51**(15): p. 4121-4131.
27. Li, B., et al., *Two dimensional modeling of momentum and thermal behavior during spray atomization of gamma-TiAl.* ACTA MATERIALIA, 1996. **44**(6): p. 2409-2420.
28. Szekely, J.T., N.J., Rate Phenomena in Process Metallurgy, 1971: p. 237.
29. Estrada, J.L. and J. Duszczyk, *CHARACTERISTICS OF RAPIDLY SOLIDIFIED AL-SI-X POWDERS FOR HIGH-PERFORMANCE APPLICATIONS.* JOURNAL OF MATERIALS SCIENCE, 1990. **25**(2A): p. 886-904.
30. Zheng, F.Z., Ming; Hu, Jiansong, Precious Metals, 1996. **17**(1): p. 28.
31. Saunders, N. and A.P. Miodownik, *CALPHAD: calculation of phase diagrams : a comprehensive guide Pergamon materials series v. 1*. 1998, NL: Pergamon Press.
32. Hillert, M., *Empirical Methods of Predicting and Representing Thermodynamic Properties of Ternary Solution Phases.* Calphad, 1980. **4**(1): p. 1-2.
33. Muggianu, Y.M., M. Gambino, and J.P. Bros, *Enthalpies of Formation of Liquid Bi-Ga-Sn Tin Alloys at 723 K--The Analytical Representation of the Total and Partial Excess Functions of Mixing.* J. Chim. Phys U6 - 1975. **72**(1): p. 83-88.
34. Belsito, D., *Review of Theory of Nucleation and Growth during Phase Separation.* 2012.
35. Z. Guo, N.S., A.P. Miodownik, J.P. Schillé, *Prediction of room temperature mechanical properties in aluminium castings.* Proceedings of the 7th Pacific Rim International Conference on Modeling of Casting and Solidification Processes, 2007.
36. D. Belsito; B. McNally; L. Bassett; V. Champagne, J.R.D.S., Jr. , *Through-Process Modeling for Cold Spray Alloy Optimization.* Proceedings MS&T 2013, 2013. **1**.
37. Osório, W.R., et al., *Electrochemical corrosion behavior of gas atomized Al–Ni alloy powders.* Electrochimica Acta, 2012. **69**(0): p. 371-378.

9 RELEVANT PRESENTATIONS & PUBLICATIONS

9.1 PUBLICATIONS

D. Belsito, B. McNally, L. Bassett, V. Champagne, Jr., R.D. Sisson, Jr., "Through-process Modeling for Cold Spray Alloy Optimization," *Proceedings MS&T 2013*, Montreal, Quebec, Canada.

D. Belsito, R. Roy, B. McNally, R.D. Sisson, Jr., V. Champagne, Jr., "Microscopic and Spectroscopic Analysis of Cold Spray Al Alloys," *Practical Metallography*, Under review.

D. Belsito, B. McNally, R.D. Sisson, Jr, "Microstructural Development in Gas Atomized Powders and Cold Spray Coatings," *International Journal of Powder Metallurgy*, In Progress.

D. Belsito, D. Apelian, M. Makhlouf, R.D. Sisson, Jr, "Method for Quantifying the Effects of Elements on Thermodynamically and Kinetically Predicted Phases," *Nature Materials* or *Acta Materialia,* In Progress.

D. Belsito, L. Bassett, B. McNally, R.D. Sisson, Jr, "Through Process Modeling of the Cold Spray Process," *Journal of Materials Processing Technology,* In Progress.

D. Belsito, B. McNally, R.D. Sisson, Jr, "Prediction of Powder Particle Mechanical Properties Using Thermodynamic, Kinetic, and Solidification Modeling," *Materials Science & Technology,* In Progress.

D. Belsito, R.D. Sisson, Jr, "Review of Nucleation and Growth Theories," *International Materials Reviews*, In progress.

9.2 TECHNICAL CONFERENCE PRESENTATIONS

D. Belsito, B. McNally, V. Champagne, Jr., R.D. Sisson, Jr., "Application of Computational Thermodynamic and Solidification Kinetics to Cold Sprayable Powder Alloy Design," Aeromat 2014, Orlando, FL, June 16-29, 2014, Submitted.

D. Belsito, B. McNally, V. Champagne, Jr., R.D. Sisson, Jr., "Through-process Modeling of Al Alloy Optimization for Cold Spray Processing," The Minerals Metals and Materials Society 2013 Annual Meeting & Exhibition, San Diego, CA, February 16-20, 2014, Accepted.

D. Belsito, L. Bassett, B. McNally, R D. Sisson, Jr., V. Champagne, Jr., "Through-process Modeling for Cold Spray Alloy Design," Center for Heat Treating Excellence Semi-Annual Meeting, Worcester, MA, December 10, 2013.

B. McNally, **D. Belsito**, V. Champagne, R.D. Sisson, Jr., "Through-Process Modeling of Cold Spray Alloy Optimization," Nanotech for Defense Conference 2013, Tucson, Arizona, November 4-7, 2013.

D. Belsito, B. McNally, V. Champagne, R.D. Sisson, Jr., "Through-Process Modeling of Cold Spray Alloy Optimization," Materials Science & Technology Conference 2013, Montreal, Canada, October 27-31, 2013.

D. Belsito, B. McNally, L. Bassett, A. Birt, R.D. Sisson, Jr., V. Champagne Jr., "Optimizing Heat Treatment of Lightweight Cold Spray Alloys with Integrated Computational Models," Submitted to Materials Science & Technology Conference 2013, Montreal, Canada, October 27-31, 2013.

B. McNally, **D. Belsito**, V. Champagne Jr. "Microstructural Analysis of Cold Sprayed Al Alloys," Cold Spray Action Team Annual Meeting, Worcester, MA, June 18-19, 2013.

D. Belsito, B. McNally, V. Champagne Jr., R.D. Sisson, Jr., "Thermodynamic and Kinetic Model-Based Processing of Light Weight Al Alloys," *Invited speaker* at 2013 North American Cold Spray Conference, Bellevue, WA, April 2-5, 2013.

D. Belsito, B. McNally, V. Champagne, Jr., R.D. Sisson, Jr., "Thermodynamic and Kinetic Model-Based Processing of Light Weight Al Alloys," The Minerals Metals and Materials Society 2013 Annual Meeting & Exhibition, San Antonio, TX, March 3-7, 2013.

D. Belsito, *A. Birt*, L. Bassett, B. McNally, M. Yang, R D. Sisson, Jr., V. Champagne, Jr., "Application of Computational Thermodynamics and Precipitation Kinetics to Cold Sprayed Al Alloy Processing & Design," Center for Heat Treating Excellence Semi-Annual Meeting, Worcester, MA, December 4-5, 2012.

M. Yang, ***D. Belsito***, R.D. Sisson, Jr., "Gas Nitriding Process Simulation for Steel Alloys," Materials Science & Technology Conference 2012, Pittsburgh, PA, October 7-11, 2012.

D. Apelian, ***D. Belsito***, "Resource Recovery and Recycling of Metals: Mini-Mills of the future," *Keynote Address* at Materials Science & Technology Conference 2012, Pittsburgh, PA, October 7-11, 2012.

D. Belsito, V. Champagne, R.D. Sisson, Jr., "Application of Computational Thermodynamics and Precipitation Kinetics to Light Weight Al Alloy Design," 13th International Conference on Aluminum Alloys, Pittsburgh, PA, June 3-7, 2012.

D. Belsito, V. Champagne, R.D. Sisson, Jr., "Alloy Design for Cold Spray Aluminum Applications," Center for Heat Treating Excellence Semi-Annual Meeting, Worcester, MA, December 5-7, 2011.

9.3 TECHNICAL CONFERENCE POSTERS

D. Belsito, B. McNally, V. Champagne, R.D. Sisson, Jr., "Application of Computational Thermodynamics and Solidification Kinetics to Light Weight Al Alloy Design," Nanotech for Defense Conference 2013, Tucson, Arizona, November 4-7, 2013. *Award: Best Poster

D. Belsito, V. Champagne, R.D. Sisson, Jr., "Center for Thermomechanical Processing of Materials by Design at Worcester Polytechnic Institute," Cold Spray Action Team Conference, October 31 - November 2012.

D. Belsito, R.D. Sisson Jr., V. Champagne Jr., "Application of Computational Thermodynamics and Precipitation Kinetics to Light Weight Al Alloy Design," First World Congress on Integrated Computational Materials Engineering, Seven Springs, PA July 10-14, 2012.

D. Belsito, V. Champagne, R.D. Sisson, Jr., Application of Computational Thermodynamics and Precipitation Kinetics to Light Weight Al Alloy Design, The Minerals Metals and Materials Society 2012 Annual Meeting & Exhibition, Orlando, FL, March 11-15, 2012.

D. Belsito, R.D. Sisson, Jr., "Modeling the Gaseous Nitriding Process in Ferritic Steel Considering Reaction Kinetics and Thermodynamics," International *Symposium* on Surface Hardening of *Corrosion Resistant Alloys,* May 25-26, 2010.

10 INDEX OF FIGURES, TABLES, AND EQUATIONS

10.1 FIGURES

10.2 TABLES

10.3 EQUATIONS

11 ACKNOWLEDGEMENTS

- **U.S. Army Research Laboratory** (Contract #: W911NF-10-2-0098) for funding and technical contributions, specifically PI Victor Champagne, Jr.

- **United Technologies Research Center** for providing powder and cold spray samples and mechanical properties analysis, specifically Aaron Nardi.

- **Advanced Materials Processing and Analysis Center** at the University of Central Florida for TEM/EDS analysis, particularly Yongho Sohn and Le Zhou.